JNeurosci
THE JOURNAL OF NEUROSCIENCE

Research Articles | Development/Plasticity/Repair

Adult-onset auditory deprivation enhances attenuation of neural responses in the visual cortex and improves peripheral visual acuity

https://doi.org/10.1523/JNEUROSCI.0690-26.2026

Received: 25 April 2026
Revised: 23 September 2026
Accepted: 27 September 2026

Copyright © 2026 Pham et al.
This is an open-access article distributed under the terms of the Creative Commons Attribution 4.0 International license, which permits unrestricted use, distribution and reproduction in any medium provided that the original work is properly attributed.

This Early Release article has been peer reviewed and accepted, but has not been through the composition and copyediting processes.The final version may differ slightly in style or formatting and will contain links to any extended data.

Alerts: Sign up at www.jneurosci.org/alerts to receive customized email alerts when the fully formatted version of this article is published.

Adult-onset auditory deprivation enhances attenuation of neural responses in the visual cortex and improves peripheral visual acuity

Katie H. T. Pham[1,2], Lukas Mesik[1,2], Rachel Lee[1], Nadia Kim[1], Shreya Vogety[1], Bomin Seo[1], Grant Dahl[1], Lia Melvin[1], Meghna Kommu[1], Rina Jeong[1], and Hey-Kyoung Lee[1,2,3,*]

1. Zanvyl-Krieger Mind/Brain Institute, Johns Hopkins University, Baltimore, MD 21218, USA.
2. Solomon H. Snyder Department of Neuroscience, Johns Hopkins University School of Medicine, Baltimore, MD 21205, USA.
3. Kavli Neuroscience Discovery Institute, Johns Hopkins University, Baltimore, MD 21218, USA.

*Corresponding Author: Hey-Kyoung Lee

(email) heykyounglee@jhu.edu

Abbreviated Title: Adult-onset deafness refines visual function

Number of pages: 53

Number of figures: 7

Number of tables: 0

Number of words: Abstract (249 words), Introduction (642 words including citations), Discussion (1496 words including citations)

JNeurosci Accepted Manuscript

Conflict of Interest Statement: The authors declare no competing financial interests.

Acknowledgements: This work was supported by the National Institutes of Health (NIH) grant R01-EY014882 to H-KL.

JNeurosci Accepted Manuscript

Abstract

The ability of the brain to undergo plastic changes throughout the lifespan of an organism is essential to optimize its interactions with its environment. Adaptation to sensory loss is observed as cross-modal recruitment of the cortical areas deprived of their own sensory inputs by the spared senses and as compensatory plasticity of the spared cortical areas. The former is thought to increase the cortical resource for processing information related to the spared modalities and the latter is thought to refine the spared senses. In animal models, synaptic and circuit-level plasticity have been observed in both the deprived primary sensory cortex and in the spared primary sensory cortices. In this study, we examined how the primary visual cortex (V1) adapts to cross-modal auditory deprivation initiated in adult mice of both sexes. To do this, we recorded the stimulus-evoked neural activity in V1 layer 2/3 (L2/3) using 2-photon calcium imaging and presented visual stimuli restricted to either the central or the peripheral visual field. We found that adult-onset deafening intensified the attenuation of stimulus-evoked responses to a range of stimuli, largely in the medial V1 representing the peripheral monocular visual field, without affecting the population decoding capability. Furthermore, adult-onset deaf mice exhibited selective behavioral improvement on peripheral visual acuity for detecting static gratings, without changes in contrast sensitivity for detecting moving gratings. Our findings suggest enhancement of neural attenuation may support compensatory plasticity in adult V1, which may benefit the stimulus encoding efficiency to improve detection of fine peripheral visual features.

JNeurosci Accepted Manuscript

Significance Statement

Losing a sensory modality leads to widespread brain adaptation to enhance the remaining senses. In addition to cross-modal recruitment, which repurposes the deprived brain areas to process the spared senses, there is functional refinement of the spared sensory areas referred to as compensatory plasticity. While plasticity is prominent for early-onset sensory loss, functional compensation is also observed after adult-onset sensory loss. Here, we report that adult-onset deafness in mice accentuates attenuation of visual cortical responses to visual stimuli, especially in the peripheral visual field, with indications of more efficient coding. Additionally, deafened adult mice show rather selective improvement on peripheral visual acuity. Our study suggests a mechanism of compensatory plasticity in the adult visual cortex, which may benefit visual function.

JNeurosci Accepted Manuscript

Introduction

It is well appreciated that losing a sensory modality leads to cross-modal adaptive plasticity across various brain areas to allow more effective use of the spared senses to guide behavior. Studies have found that two distinct plasticity mechanisms mediate such adaptation: cross-modal recruitment of the deprived sensory cortical areas by the spared senses and compensatory plasticity of the spared sensory cortices to refine their own processing (Ewall et al., 2021; Mesik and Lee, 2023). In human blind subjects, cross-modal recruitment is observed as activation of the deprived visual cortex by braille or speech, both for early- and late-onset blind (Sadato et al., 1996; Buchel et al., 1998; Burton et al., 2002; Bedny et al., 2011). There is also evidence of compensatory plasticity observed as refinement of tonotopy in the auditory cortex of blind subjects (Huber et al., 2019). Brain-wide adaptation to sensory loss is also seen in deaf human subjects with improvement in visual functions. For example, deaf subjects react faster and more accurately to visual stimuli in the peripheral visual field (Neville and Lawson, 1987; Loke and Song, 1991). However, such improvement is mainly characterized in congenitally deaf subjects and not without controversy, with reports of no difference in visual performance or even degraded performance, which seems to depend on the visual task (Bavelier et al., 2006; Kral and Sharma, 2023). Even in cases of improved visual function in deaf subjects, the neural correlates have not been clearly delineated, especially for adult-onset hearing loss. In particular, whether the primary visual cortex undergoes compensatory plasticity is unknown, although a recent study showed enhanced visually evoked responses in adult-onset deaf cats (Zhu et al., 2026).

In mice, we previously reported that adult-onset sensory loss leads to compensatory functional plasticity of the spared primary sensory cortices. For example, adult-onset visual deprivation potentiates the feedforward circuit in the primary auditory cortex (A1), including the thalamocortical synapses on layer 4 (L4) neurons (Petrus et al., 2014), and refinement of

JNeurosci Accepted Manuscript

intracortical circuits within A1 L4 and L2/3 (Meng et al., 2015; Petrus et al., 2015; Meng et al., 2017; Solarana et al., 2019). Thalamocortical synaptic plasticity in A1 is known to be limited to an early critical period (Barkat et al., 2011); hence its recovery suggests that cross-modal sensory deprivation may effectively engage latent plasticity in the adult primary sensory cortex. Furthermore, we reported that such compensatory plasticity in A1 has functional consequences at a neural level by lowering sound detection threshold and sharpening the tuning properties (Petrus et al., 2014), as well as improving auditory detection behavior especially at high frequency hearing ranges (Jendrichovsky et al., 2024). There is some evidence that similar compensatory plasticity may occur in V1 after adult-onset hearing loss. For instance, adult-onset deafness recovers thalamocortical synaptic plasticity of V1 L4 neurons and accelerates the adult form of ocular dominance plasticity (Rodriguez et al., 2018).

Here, we investigated how adult-onset deafness alters V1 L2/3 neuronal responses to various visual stimuli and whether it improves visual detection in mice. Based on human studies reporting selective improvement in the peripheral visual field, if at all, we examined neural responses in the lateral V1 representing the central visual field and the medial V1 representing the peripheral visual field. To sample neural responses to a range of visual stimuli, we used both static gratings with varying spatial frequency to assess visual acuity and moving gratings with varying contrast levels to assess contrast sensitivity. We found that adult-onset deafness exaggerated neural adaptation to repetitive visual stimulation across wider ranges of stimuli compared to age-matched controls. The refinement of neural responses was observed both for visual acuity stimuli set and moving gratings of varying contrasts, largely in the peripheral visual field. In contrast, adult-onset deaf mice only showed behavioral improvement in visual acuity in the peripheral visual field without improvement in the detection of moving gratings of varying contrast.

JNeurosci Accepted Manuscript

Materials and Methods

Animal

All experimental protocols were approved by the Institutional Animal Care and Use Committee at Johns Hopkins University. For the neural recording experiment, we used 23 C57Bl/6J mice (14 male and 9 female) around postnatal age 60 days (~P60) at the start of the experiment. Of these, 7 male (M) and 5 female (F) mice were used for the acuity stimuli recordings (CTL: 2 F, 4 M; DF: 3 F, 3 M); 7 male and 4 female mice were used for the contrast stimuli recordings (CTL: 2 F, 4 M; DF: 2 F, 3 M). For the psychophysics experiments, we used 13 C57Bl/6J mice (5 male and 8 female) and 8 cFos-TRAP2;Ai14 (6 male and 2 female) between P50~P70 at the start of the experiment. Attempts were made to balance the sexes between various groups across the different experiments, and preliminary analysis of the data did not suggest overt differences that warrant further analysis based on sex. All mice were housed in a rodent facility with a temperature range of 21–24 °C, a humidity range of 40–60%, and a 7 am/7 pm day/night cycle. All experimental mice were visually inspected to ensure healthy eyes and bodily functions.

Mouse surgery

For two-photon imaging of V1, mice underwent surgery at ~P60 for transfection of GCaMP8s virus (AAV-syn-jGCaMP8s-WPRE; Addgene#162374-AAV9) and implantation of cranial windows and headplates. At the start of every surgery, mice were anesthetized with 5% isoflurane in an induction chamber and head-fixed to a stereotaxic apparatus, where a mixture of 1-2% isoflurane and oxygen was continuously delivered throughout the surgery. The animal's breathing rate was monitored throughout the surgery to maintain a stable level of anesthesia. Next, the mice were subcutaneously injected with 2.4 µl of dexamethasone (2 mg/ml

JNeurosci Accepted Manuscript

concentration) and 10 µl atropine (0.027 mg/ml concentration) per gram of body weight. OptixCare eye gel was gently applied to the entire exposed ocular surface of both eyes using a cotton-tip applicator to protect them from dryness during the surgery. All hair covering the head was removed using a chemical hair remover (Nair), and the skin above the cortex was disinfected with iodine. This area of skin was then removed with a pair of scissors to expose the skull, which was then cleaned with 3% H_2O_2 and thoroughly dried. The loose skin above the head was glued down onto the cleaned skull using Vetbond. A circular craniotomy of 3 mm diameter was drilled out of the skull region above V1 of the left hemisphere, centered on roughly 3.6 mm posterior to bregma and 2.5 mm lateral from midline. These measurements were adjusted for the varying bregma to lambda distance of each mouse, with the assumed default being 4.21 mm. Any exposed cortical surface was temporarily covered with small pieces of sterile Gelfoam (Pfizer) soaked in sterile saline solution. In the bottom center of the exposed cortical region, 500 nL of a mixture of GCaMP8s virus diluted in sterile NaCl (1:10 dilution) was injected 0.4 mm below the pia through a pulled borosilicate glass capillary backfilled with mineral oil and angled at 0-20˚ with respect to the cortical surface. A tiny amount of Fast Green was added to the virus to enhance the visualization of the meniscus. The injection rate was maintained at 90 nl/min and repeated 3-4 times in different locations to ensure expression across a large area of V1. After each injection, the glass pipette was left in the brain for ~10 minutes to prevent backflow before being slowly retracted. After the last injection, a 3-mm diameter cover glass was placed above the craniotomy and Vetbond was applied to its perimeter to glue its edges onto the skull. A circular metal headspace was glued onto the skull using a dot of super glue placed above bregma and dental cement was applied to the region between the skull and the headplate, avoiding the cranial window. Finally, the mice received a subcutaneous injection of 20 µl of meloxicam (0.25 mg/ml solution) per body weight in grams and allowed to recover on a heat pad. Carprofen-supplemented water (70 µg/ml) was provided

JNeurosci Accepted Manuscript

for one week postoperatively to promote recovery. The injected virus was allowed to incubate for one month before two-photon imaging.

For behavior experiments, mice underwent surgery between P50~P70 for implantation of the headplate alone. The age chosen for surgery is based on the long duration needed for behavioral training to allow initiation of training around P60~P90, so the behavioral measurements could be completed before the complications of naturally occurring age-related hearing loss in C57BL/6J mice, which starts from high frequency ranges (40 kHz ≤) around P120 (Jendrichovsky et al., 2024). The surgical procedure was identical to that used for neural recording, except that GCaMP8s injections and cranial window implantation were omitted.

Ototoxic deafening

Mice were deafened at around P90-P100 for neural recording experiments and around P50~P70 for psychophysics experiments. At the start of the surgery, mice were anesthetized with 5% isoflurane in an induction chamber and placed onto a stereotaxic apparatus, where a mixture of 1-2% isoflurane and oxygen gas was continuously delivered for the entire surgery. Ear bars were not used during the procedure to allow unrestricted access to the ears. The animal's breathing rate was monitored throughout the surgery to ensure a stable level of anesthesia. Next, the mice were subcutaneously injected with 20 µl of meloxicam (0.25 mg/ml solution) per body weight in grams. OptixCare eye gel was applied using a cotton-tip applicator over both eyes, covering the entire ocular surface to protect them from dryness during the surgery. Then, the skin area surrounding the ears was disinfected with Iodine using a cotton-tip applicator. The outer ears were removed with a pair of small scissors to gain access to the middle ears. Under the dissection microscope, the ossicles inside the middle ear were removed with a fine-tip tweezer, enabling access to the cochlea through the oval window. Through the

JNeurosci Accepted Manuscript

oval window, 50 µl of kanamycin diluted in NaCl (1.76 mg/ml) was dispensed into the cochlea using a micropipette. Finally, a small piece of Gelfoam was inserted into the ear canal, and the ear was sutured closed. The animals were then placed on a heating pad to recover from anesthesia and provided with carprofen water (70 µg/ml) for 7 days to promote recovery. Three days after the initial surgery, the animal was briefly anesthetized on the same stereotaxic setup for the removal of the suture and Gelfoam from both ears. Vestibular damage, which manifested as an abnormal head tilt or locomotion, was noted in a few mice shortly after recovery from anesthesia. These mice were euthanized and were not used for experiments.

Intrinsic Signal Imaging

Retinotopic mapping was performed using an intrinsic signal imaging protocol adapted from the Callaway lab to find the cortical areas that best correspond to the peripheral and the central field, as well as define the border that separates V1 from the higher order visual areas (HVAs) (Garrett et al., 2014; Juavinett et al., 2017). Each mouse was induced into anesthesia with 5% isoflurane. The mice were administered 5 µl of sedative chlorprothixene (0.2 mg/ml concentration) per gram of body weight as needed, to allow for a lower isoflurane concentration (< 1%) during imaging. Mice were then transferred to a heated pad, and their heads were secured under a CCD camera for imaging of the V1/HVA regions through the cranial window. The skull was illuminated with red light, and a contrast-reversing drifting checkerboard pattern stimulus, moving at a set rate, was presented to the mouse on a screen 10 cm from the contralateral eye. As this stimulus pattern is being presented to the mouse, the response to each image pixel was acquired, and a Fourier transform was performed to extract signal components at the stimulus frequency. The computed phase maps were converted into retinotopic coordinates, and the borders of the visual areas were identified based on retinotopic reversals between areas using an automated algorithm. Using this method, area segmentation

JNeurosci Accepted Manuscript

is performed by an algorithm that identifies visual areas based on whether their retinotopy is mirror- or non-mirror-symmetric with respect to the visual space in the retina. This visual area map was then overlaid on an acquired image of the vasculature to allow for the identification of V1 and surrounding HVAs. The mice were then allowed to recover on the heated pad and returned to the animal colony.

2-Photon Ca^{2+} imaging of neural activity

During two-photon imaging, the mice were awake, head-fixed on a cradle to which they were habituated over 3 sessions prior to the first recording. Calcium imaging was performed on a custom-built 2-photon microscope based on the Janelia MIMMS design. Images were acquired at 30-Hz and 512 x 512 pixel resolution (field of view: ~500 x 500 μm^2) using 30–100 mW of laser power depending on the depth and strength of the viral expression. A 27" screen was positioned 30 cm from the right eye and angled so that the central stimulus sits directly in front of the mouse **(Figure 1A).** The height of the screen was adjusted so that the middle of the screen's height was at the same level as the pupil. Screen settings were adjusted to 100% brightness, mean luminance of 35 cd/m^2, and a 144 Hz refresh rate. The position of the central stimulus was 0-10˚ azimuth, which is within the binocular visual field of mice **(Figure 1A)**. The position of the peripheral stimulus is 80-90˚ azimuth, which is in the periphery of the monocular visual field **(Figure 1A)**. Because both eyes were open during the experiment, the central stimuli will be viewed through both eyes; hence, the neural responses measured in the lateral binocular V1 is expected to be summation of responses from both eyes. The stimulus is presented on a gray isoluminant background, which remains on the screen throughout the recording session. All visual stimuli were generated using the Psychtoolbox-3 extension of Matlab (Brainard, 1997). For each recording day, we recorded from 2 lateral and 2 medial regions of V1. The stimulus location varies with the recording region: the peripheral stimulus was shown during medial

Neurosci Accepted Manuscript

recordings, and the central stimulus was shown during lateral recordings. During acuity measurements, static sinusoidal gratings were presented at 100% contrast and 90° orientation, at spatial frequencies of 0.1, 0.3, 0.5, 0.7, 0.9, and 1.1 cycles per degree (cpd). During contrast level measurements, downward-drifting sinusoidal gratings were presented at a spatial frequency of 0.05 cpd, a temporal frequency of 2 Hz, and a 90° orientation, at contrast levels of 4, 8, 16, 32, 64, and 85%. Each acuity recording session was structured to include about 70 trials, and each trial consisted of 300 ms of a single stimulus presentation, followed by ~4.7 s of intertrial interval (ITI). Each contrast recording session was structured to include 70 trials, each comprising 1.3 s of stimulus presentation followed by ~6.3 s of ITI. Each stimulus type was shown 10 times, and the stimulus sequence was completely randomized, with 10 blank trials consisting solely of the isoluminant background interspersed amongst them. The same sequence was presented for all recordings of all mice. Each day of recording, therefore, contained 4 recording sessions: 2 central visual field stimulation sessions (recording from the lateral V1) and 2 peripheral visual stimulation sessions (recording from the medial V1). The cortical locations recorded on the first day were approximately returned to in subsequent days, but we did not record from the same set of cells. The responses of the pre-deaf and post-deaf recordings were averaged by recording type across two consecutive days to reduce day-to-day activity fluctuations. The output of the neural recordings was stored as folders of TIFF files for subsequent processing. A custom-built Raspberry Pi NoIR camera was positioned in front of the left eye to collect pupil location and diameter data throughout the neural recording sessions. The pupil data were recorded at 25-30 Hz and stored as .h264 video files.

JNeurosci Accepted Manuscript

Analysis of neural data

Raw TIFF files were processed using the Suite2p (Pachitariu et al., 2016) (https://github.com/MouseLand/suite2p) for motion correction and region of interest (ROI)

detection. Images were registered using non-rigid motion correction (block size: 128 x 128, max shift: 5 pixels). ROIs were identified using the functional segmentation method with a threshold scaling of 1.0, and pixels were classified as ROI or neuropil using a 25-pixel spatial high-pass filter. For each ROI, the suite2p program extracted the raw fluorescence traces and neuropil traces, which were subsequently exported to MATLAB for further analysis.

In MATLAB, a custom script was written to identify stimulus-evoked responses for each Suite2p-identified ROI from each recording. First, trial onsets were determined by calculating the cumulative frame count for each TIFF file (ops.frames_per_file). Neuropil decontamination was performed using the formula: $Fcorr = F - 0.7 \times Fneu$, where *Fcorr* is the neuropil-corrected fluorescence value, *F* is the soma fluorescence value, and *Fneu* is the neuropil fluorescence value. Using the *Fcorr* traces, relative fluorescence changes ($\Delta F/F_0$) were calculated for each ROI in each trial. The baseline fluorescence (F_0) was defined as the mean activity during the 1-second (30 frames) window immediately preceding the trial onset. The change in F (ΔF) is *Fcorr*- F_0. Trials were sorted and grouped according to a pre-defined random sequence of spatial frequencies or contrast levels. Visual responsiveness was determined for each neuron using the distribution of mean response values during the window of 2 seconds (60 frames) post-onset for each spatial frequency or 3 seconds (90 frames) for each contrast level, which was compared against the distribution of responses to blank control trials of the same recording session using a right-tailed Wilcoxon rank-sum test. Neurons were classified as responsive if their p-value was less than the Bonferroni-corrected p-value of 0.00833 and the trial-averaged peak $\Delta F/F_0$ exceeding a threshold of 0.15. ROIs in which the maximum $\Delta F/F_0$ was higher than 8 were excluded from further analysis, as these were invariably ROIs in which the baseline fluorescence dropped too close to 0. For each ROI, single-trial $\Delta F/F_0$ traces corresponding to the same stimulus condition were aggregated and averaged to generate a mean response trace for that specific spatial frequency. The post-onset peak and the area-under-the-curve (AUC) of

JNeurosci Accepted Manuscript

these traces were also computed and averaged across recordings of the same experimental condition (pre vs. post; CTL vs. DF). The proportion of responsive cells was calculated by dividing, for each recording, the number of cells obtained after the previous statistical filtering by the total number of cells picked up by Suite2p.

Decoding of neural data

Neural decoding was implemented using the Neural Decoding Toolbox (Meyers, 2013). We employed a Maximum Correlation Coefficient Classifier to perform binary classification between background and a specified stimulus condition. $\Delta F/F_0$ traces were binned using a 5-frame sliding window with a 2-frame step size to create a temporal series of population vectors. A 5-fold cross-validation was used. Decoding accuracy was quantitatively determined by computing the peak accuracy, which is the maximum percentage of correct classifications observed in the post-stimulus-onset period, and the Area Under the Curve for decoding accuracy above chance level (50%) was calculated using the trapezoidal rule within a 60-frame (2 s) stimulus window post-onset for acuity stimulus and a 90-frame (3 s) stimulus window post-onset for contrast stimulus. In addition, we calculated the d-prime (*d'*) for the decoding data using decoding accuracy before versus after stimulus onset of each recording session as: $d' = \frac{\mu_{before} - \mu_{after}}{\sqrt{0.5 \times (\sigma_{before}^2 + \sigma_{after}^2)}}$, where μ and σ are, respectively, the mean and standard deviation of each dataset. Decoding accuracy before onset was taken at time bin corresponding to ~0.133 s (1 to 5 frames) before stimulus onset. Decoding accuracy after onset was taken to be the value at the time bin with peak decoding accuracy after stimulus onset of each recording.

Contrast sensitivity (C50) computation

JNeurosci Accepted Manuscript

A custom MATLAB script was used to fit each ROI's average response to each stimulus over the course of the recording session to determine the contrast percentage at half-max response of each ROI. The secant slope of the curve was also computed to determine the steepness of the ROI's rising phase from a low-contrast response to a high-contrast response. The fitting utilizes a Naka-Rushton function with four parameters: $R(C) = Rmax \times \frac{(C^n)}{(C^n + C50^n)} + b$, where *Rmax* is the maximum neural response, C50 is the contrast level at half-max response, *n* is the Hill coefficient that represents the steepness of the curve's slope, and *b* is the baseline spontaneous neural activity at 0% contrast. The 2-photon calcium imaging neural data are input as an N x 7 matrix, where each N is the vector of a ROI's responses, and each of the 7 columns represents the 6 contrast stimuli + background, which are taken to be 0% contrast. Prior to the fitting, lower and upper bounds, as well as initial guesses, were set for each parameter within reasonable bounds, and the same setting was used for all of the curve-fitting. The lsqcurvefit function was used to perform the fitting, with each of the four parameters adjusted over up to 2,000 interactions to minimize the difference between the model and the real data. A standard goodness-of-fit (R^2) was computed using this formula: $R^2 = 1 - \frac{SST}{SSE}$, where *SST* is the Total Sum of Squares and *SSE* is the Sum of Squared Errors. All ROIs with R^2 less than 0.8 were filtered out due to poor fit. ROIs whose fitted curves failed to reach at least 90% of their theoretical maximum by 85% contrast were also excluded because they were non-saturating. The secant slope of the fit was computed using the response at 10% and 90% of saturation (C10 and C90, respectively) using this formula: $Slope = \frac{0.8 \times Rmax}{C90 - C10}$. The average values and the average slope of the remaining ROIs were computed for comparison across experimental conditions.

Pupil size and pupil location analysis

Neurosci Accepted Manuscript

Pupil videos were converted to .avi files using ffmpeg before being uploaded to Deeplabcut (DLC). For each video within DLC, 20 frames were extracted using the uniform algorithm and manually labeled at 4 positions (top, bottom, anterior, and posterior) to delineate the pupil boundary. Labeled frames were split into training and test sets, and the network was trained for 50,000 to 100,000 iterations. The resulting model was used to analyze the video from which it was built. This was repeated for each video to collect the estimated pixel coordinates of each of the four pupil labels over the course of the recording session. This DLC output was imported into Python, filtered by excluding estimates with likelihood values below 0.9, and then a median filter was applied to reduce frame-to-frame jitter in the coordinate trajectories. The pupil diameter was calculated for each frame by inputting the anterior and posterior coordinates into the formula: $distance = \sqrt{(x_2 - x_1)^2 + (y_2 - y_1)^2}$, where (x_1, y_1) and (x_2, y_2) representing their pixel coordinates, respectively. Likewise, pupil center coordinates were calculated by inputting the anterior and posterior coordinates into the formula: $midpoint = (\frac{x_1+x_2}{2}, \frac{y_1+y_2}{2})$.

Afterward, outliers were removed from the pupil diameter dataset using the Mahalanobis distance method with a probability threshold set to the third interquartile range (IQR) point of all Mahalanobis distances calculated for each point, with minor manual adjustments. To determine the stimulus-evoked change in pupil size, we first temporally aligned the pupil trace with the neural trace from the same recording session. The frame-rate differences were accounted for by applying a linear interpolation to the pupil trace using the numpy interp function in Python. Next, the aligned pupil trace was segmented into individual trials aligned to the stimulus onset time. This was done similarly to segmenting the neural trace from a recording session into individual trials. For each trial, the pupil diameter was calculated as the average pupil size during stimulus presentation. These values, grouped by stimulus condition, were normalized to the average pupil size of the background stimulus trials from the same recording to account for minor variations in video zoom settings and camera locations.

JNeurosci Accepted Manuscript

To determine the pupil movement using the pupil center x-y coordinates, the trajectory map of pupil center location during each session was generated. The trajectory map for each session was then converted into a spatial density map using a 2D kernel density estimation (MATLAB ksdensity function). Density estimates at each grid point (120 x 120 grid) were scaled by the number of points to yield values in points per unit area. Average density maps for central visual stimuli presentation and peripheral visual stimuli presentation were then generated for each day (2 sessions each). To assess statistical significance between the pupil center density maps for central and peripheral visual stimuli, we used a nonparametric permutation test. All individual density maps were pooled together, and group labels were randomly reassigned to two groups. For each permutation (n = 1000), a difference map was generated and the maximum absolute differences across all grid points were recorded to generate a null distribution of maximal differences. Statistical significance was determined when the observed density within each grid of the difference map was greater than the 95% threshold ($\alpha = 0.05$). None of the average density maps for a pair of central and peripheral stimuli presentation sessions obtained on the same day showed statistical significance using this criterion. In addition, the Pearson correlation coefficient between mean density maps of central and peripheral visual stimuli was calculated for sessions of each day, which was then compared using a nonparametric 2-way ANOVA (aligned rank transform, ART; see below for details) for interaction between condition (CTL vs. DF) and time (pre vs. post).

Visual detection experiment

For habituation, mice were handled by the experimenter, with the duration of contact gradually increased each day over 3-4 days before the first day of the experiment. After the handling stage, the mice were head-fixed in the experimental rig to habituate to the setup over 3-4 days, with the duration of head fixation gradually increasing each day. Water deprivation

JNeurosci Accepted Manuscript

began on the first day of handling, and ~1 ml of 5% sucrose solution was administered to each mouse daily by completing the behavior tasks, placing it in a small saucer in its home cage, or a combination of both. Liquid dispenser used during the behavior task was built using a solenoid valve (PreciGenome) controlled by a custom Arduino script. Lick detections were done by measuring a small electrical current generated when licks closed an electrical circuit between the water dispenser and the cradle where the mouse sits. After habituation to the setup, the mice underwent a passive training phase in which 5-10 µl of 5% sucrose was automatically delivered upon stimulus presentation to establish an association between visual cues and reward. Once this association was learned, active training was introduced, in which sucrose was dispensed only when mice licked the port in response to stimulus detection within a period after stimulus onset. The experiment was conducted in a lightproof, soundproof rig comprising a cradle, a 27” computer screen, a lick port, and a Raspberry Pi camera. The lick port was positioned in front of the mouse, allowing the distance between the mouse and the lick port to be adjusted to manage the licking behavior. The computer screen was placed 24 cm from the mouse's right eye, and the screen settings were adjusted to 0% brightness, mean luminance of 23.5 cd/m^2, and 144 Hz refresh rate. The camera was positioned to the left of the lick port to observe the mouse’s licking behavior from outside of the rig. Custom Arduino and MATLAB programs were used to conduct the experiment and collect data. Psychtoolbox was used to construct the visual cues. During the classical conditioning part of the experiment, full-field drifting square wave gratings at 100% contrast and 0.05 cpd were presented. During the operant condition phase of the experiment, drifting sinusoidal gratings of varying contrast levels and static square wave gratings of varying spatial frequencies were used. Both types of gratings were presented at 90˚ orientation and restricted to the central or peripheral field, depending on the trial. The contrast levels range from 1% to 85%. All contrast stimuli were set to have a spatial frequency of 0.05 cpd, a temporal frequency of 2 Hz, and a downward movement trajectory. The spatial frequency stimuli had cpd values ranging from 0.05 to 1.0. All spatial

JNeurosci Accepted Manuscript

frequency stimuli were maintained at 100% contrast. Both types of stimuli were embedded on the gray isoluminance screen. The stimulus was presented either in the central (10-20˚ azimuth within the binocular visual field, see **Figure 1A**) or the peripheral (90-100˚ azimuth in the monocular visual field, see **Figure 1A**) visual field, depending on the trial. Each day, the mice complete ~180 trials. For each day, a range of stimulus levels was selected for testing based on the previous day's performance, and while the sequence of stimulus presentation was random, the number of times each stimulus was presented over the course of a session was ensured to be equal. The peripheral and central stimulus was presented on alternating days. Sometimes a 'period without licking' was required between trials to reduce random licking behavior as needed. When this was active, the subsequent trial was initiated only if the mouse had refrained from licking the port for a specified duration (about 2~8 s). To prevent mice from anticipating rewards based on a fixed inter-trial interval and to ensure that licking behavior was driven solely by operant conditioning, a randomized time jitter (up to ± 3 sec) was added to both the trial initiation interval and the period without licking. When task engagement dropped, 'free reward after N misses' was activated, dispensing 5-10 µl of 5% sucrose water after a predetermined number of consecutive unsuccessful trials.

The mouse achieved a 'hit' and received reward if it licked within a 1-s window following the stimulus onset, defined as the response window (*Res*).To evaluate the stimulus-specific performance, we calculated the detection rate (sometimes also referred to as guessing-corrected hit rate) as: $Detection\ rate = \frac{(HR-Bkg)}{(1-Bkg)}$, where *HR* is the stimulus-specific hit rate, and *Bkg* is the background lick rate, the fraction of total trials with any licking within the 1-s window before stimulus onset. As an alternative performance metric, we also calculated the behavioral d-prime (*d'*) using: $d' = norminv(HR) - norminv(Bkg)$, where *norminv* is the inverse of the normal cumulative distribution. For the purpose of *d'* calculation, we used $HR = \frac{(number\ of\ hits)+0.5}{(number\ of\ trials)+1}$ to prevent *d'* from going to infinity with perfect performance. For each day's

JNeurosci Accepted Manuscript

session, detection rates for each visual stimulus category (for acuity data set: cycles per degree (cpd) range; for contrast data set: %contrast range) were fitted with a logistic function: $f(x) = \frac{1}{1+\exp(-\frac{x-a}{b})}$, where *a* and *b* are curve fit coefficients. From this equation, the detection threshold, which is the visual stimulus value (*x*) that yields 50% detection rate, was calculated for each day's performance. Detection threshold improvement across days of training was plotted and fitted using a sigmoid function: $f(x) = base + \frac{max}{1+\exp(\frac{xhalf-x}{rate})}$, where *base* is the baseline value, *max* is the amplitude, *xhalf* is the *x* value at half maximum, and *rate* is the slope. Training sessions were terminated once detection performance plateaued, which indicated sufficient learning. For each mouse, average detection rates of the last 5 sessions for each visual stimulus were plotted and fit by the logistic function, which was then used for calculating the average detection threshold (the same as detailed above) for each mouse.

Immunohistochemistry

To confirm successful deafening, the cochlea of mice that contributed to the final dataset was extracted for histological analysis. For fixation, 0.5 ml of 4% formaldehyde solution was injected through the oval window, followed by submersion in 2 ml of 4% formaldehyde for two hours on a low-speed shaker at room temperature (RT). The cochlea was subsequently washed with PBS and then decalcified in 10-15 ml of 5% ethylenediaminetetraacetic acid (EDTA) for 48 hours at RT. After decalcification, the cochlea became spongy and was washed in phosphate-buffered saline (PBS, pH = 7.4) and immersed in 1 ml of 30% sucrose solution overnight at 4°C. Finally, the cochlea was then manually sliced into the basal, medial, and apical coils. To assess damage across the tonotopic gradient, following slicing, cochlear sections were stained with DAPI and Alexa Fluor 488-phalloidin (1:200, Life Technologies, Cat#A12379) to visualize cellular structure. Stained samples were mounted on glass slides with ProLong™ Gold Antifade

Neurosci Accepted Manuscript

mounting solution (Life Technologies, Cat#P36930) and imaged using a fluorescent confocal microscope (Zeiss LSM 700). Images of the basal, medial, and apical sections of the cochlea were processed with ImageJ FIJI software to assess hair cell integrity across the cochlea's tonotopic axis.

Experimental Design and Statistical Analyses

All statistical analyses were performed in either GraphPad Prism, R, or MATLAB. All data were first processed in MATLAB (MathWorks) and converted into tables in CSV format for import into R or RStudio (https://www.r-project.org) for statistical analysis. The distribution of the data was assessed for normality using the Shapiro-Wilk test. Non-parametric neural data were analyzed by the Aligned Rank Transform (ART) method using the ARTool package in R (Wobbrock et al., 2011). The method consisted of first applying the aligned rank transform on the data and then fitting a linear mixed-effects (LME) model on the rank-transformed data. For each experimental condition, we assess the significance of the interaction between the two factors stimulus and time, treating the animal as a random effect. Following significant results, post hoc pairwise comparisons were performed on ART-aligned data to determine which stimulus conditions yielded significant differences in neural activity between the two time points. The degrees of freedom were approximated using the Kenward-Roger method, while the p-value adjustments were done using the Holm method. Parametric pupil data were analyzed using "nlme" package in R Studio to assess the significance of the interaction between the two factors stimulus and time, while also treating the animal as a random effect. In both cases, "pbkrtest.limit" and "lmerTest.limit" were set to 10,000 to enable degree of freedom (d.f.) calculation for the large number of observations. For statistically comparing pairs of pupil center

JNeurosci Accepted Manuscript

location density maps of central and peripheral sessions from each mouse obtained each day, we used the permutation test in MATLAB as detailed above. The observed mean difference and the absolute observed mean difference were compared to the permutation threshold ($\alpha = 0.05$) to determine statistical significance. Parametric behavioral data were statistically compared using 2-way ANOVA using the GraphPad Prism software. Data were presented as mean ± SEM (standard error of the mean), except when noted as median ± IQR (interquartile range). Significance was reported as *$p < 0.05$, **$p < 0.01$; ***$p < 0.005$. Effect sizes for nonparametric paired data sets were estimated using the matched-pairs rank-biserial correlation (r) method, and for parametric data sets Cohen's d was used.

Code accessibility

All custom-made MATLAB and R scripts will be made publicly available in Mendeley Data (https://data.mendeley.com) upon publication (doi: 10.17632/5556vjvfbg.1).

Data accessibility

Data sets used in this manuscript will be made publicly available in Mendeley Data (https://data.mendeley.com) upon publication (doi: 10.17632/5556vjvfbg.1).

JNeurosci Accepted Manuscript

Results

To investigate how deafening modulates visually-evoked population responses in V1 L2/3, we used 2-photon calcium imaging to record neural activity in response to visual stimulus presentation. Upon reaching P60, C57BL/6J mice had GCaMP8s injected into their left primary visual cortex and a 3-mm circular cranial window implanted over it. Following a 1-month incubation period, the mice were habituated to the experimental setup, and a baseline stimulus-evoked response was recorded. To minimize day-to-day variation in neural responses, the baseline recording process was performed over two days, and the data from both days were averaged. This was immediately followed by the deafening procedure for half of the mice, splitting the animals into the control (CTL) and deaf (DF) groups. After a week, 2 days of "post" recordings were performed with the exact procedure as the baseline "pre" recordings (**Figure 1A, B**). Since V1 is topographically organized, recordings were done in the medial V1 during sessions with visual stimuli presented in the peripheral visual field and in the lateral V1 during those with central visual stimuli. The borders of V1 were delineated using intrinsic signal imaging of V1 through the cranial window (Schuett et al., 2002; Juavinett et al., 2017) before the first day of the baseline (pre) recording. The visual sign field (VSF) map obtained from the intrinsic signal imaging was overlaid on the image of V1 vasculature, which was used as landmarks to locate the medial (within the monocular zone representing the peripheral visual field) versus lateral (within the binocular zone representing the central visual field) regions of V1 for recording neural responses (**Figure 1C, D**). We used 2 sets of visual stimuli: one to assess spatial acuity and another to measure contrast sensitivity. Both sets of stimuli spanned 10 degrees of azimuth and were presented at either the central visual field (0-10˚ azimuth) within the binocular visual field or the peripheral visual field (80-90˚ azimuth) in the monocular visual field, depending on the session (**Figure 1A**). The acuity stimulus comprised static horizontally oriented sinusoidal gratings of fixed contrast with varying spatial frequencies, while the contrast

JNeurosci Accepted Manuscript

stimulus was horizontal sinusoidal gratings of a fixed spatial frequency at varying contrast and drifting from top to bottom at a fixed speed (see Methods for details). For both sets, the different stimulus levels presented within the same recording session were presented randomly, but in equal proportions, and identical sequences were used for the pre and post recording sessions as well as across different animals (**Figure 1E**).

Adult-onset deafening results in greater attenuation of V1 L2/3 neural responses to spatial acuity stimuli presented in the peripheral visual field

We first examined whether adult-onset deafening alters V1 L2/3 neural activity to spatial acuity stimuli presented in the central or the peripheral fields. In control mice, we observed the largest neural responses to the lowest spatial frequency grating used (0.1 cpd) for both visual fields (**Figure 2A**). This is consistent with previous investigations showing that V1 neurons of mice are most sensitive to the spatial frequency range of 0.05 to 0.2 cpd (Histed et al., 2012). In CTL mice, the response size, measured either as the peak response within a 2-second window after the stimulus onset or the area under the curve (AUC) of the Ca^{2+} transients within this time window, remained similar between pre and post sessions for visual stimuli presented in the central visual field (**Figure 2A-D**), but there was significant attenuation of responses to spatial frequencies of 0.5 and 0.7 cpd presented in the peripheral visual field during the post recording sessions (**Figure 2C, D**). The attenuation observed in the post recordings is consistent with previous studies. In humans, non-human primates, and mice, repeated exposure to the same visual stimuli has been reported to attenuate neural activity, which has been thought to encode familiarity and promote novelty detection (Grill-Spector et al., 2006; Homann et al., 2022; Lopez-Ortega et al., 2024).

JNeurosci Accepted Manuscript

In adult mice deafened for 1 week (DF), we also observed the largest response to the lowest spatial frequency grating used (0.1 cpd), but there was a greater degree of attenuation of responses in the post sessions (**Figure 2A-D**). Unlike in CTLs, we observed attenuation of responses to some of the higher spatial-frequency stimuli presented in the central visual field (0.7 and 1.1 cpd), as well as attenuation of responses to peripheral stimuli evident from 0.3 cpd (**Figure 2 C, D**). This suggests that adult-onset deafening shifts the range of neural response attenuation to visual stimuli that normally produce larger responses under the naïve baseline condition. Attenuation of neural responses we observed across days was not accompanied by within session reduction in neural responses **(Supplementary Table 1)**, likely due to the small number of each stimulus repetition (10 trials each), and suggests that attenuation develops across days.

Attenuation of population activity is not accompanied by a decrease in decoding capability for spatial acuity stimuli

To determine whether the attenuation of neural responses in the post recording sessions was due to fewer visually responsive cells, we quantified both the number of total and responsive cells in each imaging view field, which was about 500 x 500 μm^2, and quantified the proportion of responsive cells accordingly. Previous findings reported that only a fraction of V1 L2/3 neurons (~20%) have a preferred horizontal orientation (Hoy and Niell, 2015); hence it was not surprising to find the proportion of responsive cells lower than this estimate, given the static and spatially restrictive nature of our stimuli. We did not find a statistically significant difference in either the total number of cells, the number of responsive cells, or the proportion of responsive cells identified in each view field between the pre and post recording sessions for CTL and DF groups (**Figure 3A**). This suggests that the attenuation of responses seen during the post session is not due to sampling fewer cells or having fewer responsive neurons.

JNeurosci Accepted Manuscript

Next, we examined whether the attenuated population neural responses to acuity stimuli negatively affect the population's decoding capability. Based on our observation that adult-onset deafening significantly attenuates responses to 0.3 and 0.5 cpd stimuli in the peripheral field, we tested the accuracy of V1 L2/3 population responses to decode these stimuli against background-only trials using a Maximum Correlation Coefficient decoding paradigm (Meyers, 2013) (see Methods for details; **Figure 3B**). We quantified the decoding accuracy of each recording as the post-stimulus onset peak accuracy and the 2 seconds post-stimulus onset integrated accuracy, computed as the area under the curve above the 50% chance accuracy. For both metrics, we found no significant difference in decoding accuracy between pre and post recording sessions in any of the experimental groups for either the 0.3 or 0.5 cpd stimuli. As expected, the integrated decoding accuracy of 0.5 cpd is lower than that of 0.3 cpd (**Figure 3C**). We confirmed good decoding accuracy by calculating d-prime (*d'*) values for peak accuracy (see Methods; $d' > 1.6$, see **Figure 3B** legend for exact values). Collectively, our results suggest that the attenuated responses to acuity stimuli in the peripheral visual field observed after adult-onset DF do not negatively impact the ability to decode stimulus information from the population responses of V1 L2/3 neurons.

Adult-onset deafening results in greater attenuation of V1 L2/3 neural responses to contrast stimuli presented in the peripheral visual field

Next, we examined whether adult-onset deafening alters V1 L2/3 neural responses to stimuli of different contrast levels of moving gratings presented at central or peripheral locations. In control mice, we observed the largest responses at the highest contrast level (85%) in both visual fields (**Figure 4A-D**). This is consistent with previous findings of increasing contrast levels eliciting stronger responses in the visual cortex (Niell and Stryker, 2008; Camillo et al., 2020). The contrast stimulus-evoked response in CTL mice, computed as the peak response within a

JNeurosci Accepted Manuscript

3-second window after stimulus onset or the AUC of the Ca^{2+} transients within this time window, remains largely unchanged between the pre and post recording sessions, except some response adaptation observed at the 16% contrast level in the central visual field and increased responses at the 85% contrast level in the peripheral visual field.

In the DF mice, on the other hand, there was widespread attenuation of visually evoked responses to stimuli in both visual fields. In the central visual field, the attenuation in response was significant for 8% and 16% contrast levels. In the peripheral visual field, the attenuation in response was significant for 8%, 16%, and 64% contrast levels, with 32% contrast response not reaching statistical significance despite a similar magnitude of attenuation. This suggests that adult-onset DF triggers attenuation of responses across a range of middle-contrast levels, with the range being wider in the peripheral visual field (**Figure 4C-D**). Similar to what we observed with acuity stimuli, attenuation of neural responses to contrast stimuli were largely not observed within a session, except for a moderate decrease in responses to 64% contrast presentation in the peripheral visual field of CTL mice **(Supplementary Table 2)**.

Attenuation of population activity is not accompanied by a decrease in decoding capability or a change in contrast sensitivity

Similar to the acuity stimulus recordings, we examined whether the observed adaptation to contrast stimuli resulted from a loss of visually responsive cells in the post recording sessions. Quantification of the proportion of responsive cells within each recording, using a method similar to that used before, did not yield any significant decrease in total cell counts, responsive cell counts, or the proportion of responsive cells (**Figure 5A**). Previous findings reported that ~40% of adult V1 L2/3 neurons respond to drifting gratings and given that ~20% have a preferred horizontal orientation (Rochefort et al., 2011; Hoy and Niell, 2015), it is

JNeurosci Accepted Manuscript

expected that ~8% of V1 L2/3 neurons would be responsive to drifting horizontal gratings. This estimate matches closely with our observed proportion of responsive neurons. The preserved proportion of responsive neurons across the experimental conditions suggests that the observed attenuation of the population response was due to mechanisms other than a decrease in the number of visually responsive cells.

We next examine how such attenuation in the V1 L2/3 population response affects its decoding capability. We tested the population's ability to decode stimuli at contrast levels ranging from 8% to 64% in the peripheral visual field, where we observed the most prominent decline, using the same method described for the acuity stimuli (**Figure 3**). We quantified the decoding accuracy of each recording as the 3-second post-onset peak accuracy and the 3-second post-onset integrated accuracy. Neither metric demonstrated a significant change in decoding capability due to deafening-evoked attenuation between the CTL and DF groups (**Figure 5B, C**). By calculating d-prime (*d'*) values for peak decoding accuracy (see Methods), we confirmed robust decoding ($d' > 2$; see **Figure 5B** legend for exact values). This suggests that the population's decoding capability remains intact despite large attenuation in neural responses.

Finally, we examined the effect of DF on the contrast sensitivity of neurons. While some V1 L2/3 neurons are reportedly tuned to a particular contrast, most of the population are thought to monotonically increase their firing with increasing contrast (Durand et al., 2016). Such an increase in firing magnitude has traditionally been modeled using a Naka-Rushton function, in which response intensity is plotted as a function of contrast percentage, and the contrast level at half-max response can be quantitatively determined and compared across different animal groups (Camillo et al., 2020). To quantify the effect of population response attenuation on neuronal contrast sensitivity, we fitted the response of each neuron to varying contrast levels using the Naka-Rushton function and determined the contrast level at half-max response (C50)

JNeurosci Accepted Manuscript

as well as the slope of the rising phase between 10% and 90% contrast (see Methods for details). In CTL mice, the average fitted curves, C50, and slope were highly similar between the pre and post recording sessions in both the central and peripheral visual fields. In DF mice, there was no significant change in C50, which is a measure of contrast sensitivity, even though the average fitted curve shifted downward, reflecting response attenuation. Despite the magnitude of the decline in the slope of the fitted curve, the reduction did not reach statistical significance (**Figure 5D-E**). Overall, our data support the conclusion that V1 L2/3 neuronal contrast sensitivity remains unchanged despite response attenuation.

Pupil size and location remain unchanged with visual stimuli onset or location of stimuli

It is well established that neural activity varies across arousal states, which could contribute to the attenuation of neural responses across days. One commonly used proxy for arousal is pupil size, which enlarges with increasing arousal (Vinck et al., 2015; Durand et al., 2016; Neske et al., 2019). To determine whether arousal state is a factor to consider when interpreting our neural recording datasets, we analyzed pupil diameter and location from video recordings of the eye that was not viewing the visual stimuli (**Figure 1A**). To our knowledge, movement and dilation of the rodent's pupil are largely synchronized between the two eyes and are controlled by both the pupillary reflex in response to changes in luminance and by neuromodulation (Larsen and Waters, 2018; Viglione et al., 2023; Lapanja et al., 2025). Pupil videos collected using a custom-built Raspberry Pi camera were analyzed using the DeepLabCut pose estimation toolbox (Mathis et al., 2018; Privitera et al., 2020) (see Methods for details), and the anterior-posterior labels of the pupil in each frame were used to compute the pupil diameter and the pupil center location throughout the entire experiment duration (**Figure 6A**). This was then aligned with the stimulus onset, enabling examination of changes in pupil size and pupil center location across trials. When changes in pupil size were aligned to the

Neurosci Accepted Manuscript

667 stimulus onset and analyzed on a per-trial basis, we did not detect any noticeable stimulus-
668 evoked dilation or constriction. When we averaged them within the same stimulus trial types and
669 across different animals under the same experimental conditions, we also did not detect any
670 significant change following stimulus onset (**Figure 6B**). This is expected given that the visual
671 stimuli were isoluminant to the background, restricted to a small portion of the visual field, and
672 presented passively.

673 To determine whether pupil diameter changes with stimulus levels and from pre to post
674 recording sessions, we computed the average pupil size during stimulus presentation for each
675 trial and averaged these values within each trial type. To account for variation in video recording
676 conditions across different days, before combining averages across recordings for the same
677 experimental condition, we normalized each trial's pupil size to the average pupil size during the
678 background trials of the same recording session. When comparing normalized pupil size across
679 stimulus levels and changes from pre to post recordings at the same stimulus level, we did not
680 find a significant difference for any experimental condition or stimulus type (**Figure 6C, D**).

681 Lastly, we tracked the pupil location throughout the experiment. Eye movement in mice
682 are relatively small (~5˚) and mostly linked to head movement (Meyer et al., 2020); hence it is
683 not considered a major contributor that can shift the gaze of head-fixed mice to drastically
684 change the perceived location of the visual stimuli. However, since visual responses in mouse
685 V1 can be modulated by gaze and head direction (Parker et al., 2022), we want to confirm that
686 there were no drastic changes in pupil center location. Moreover, depending on where along the
687 vertical axis the mice focused, there could also be complications from the effect of a higher
688 spatial-frequency cutoff at higher elevations (Zhang et al., 2015). We computed the pupil center
689 coordinates from the DeepLabCut outputs and generated their 2D trajectory over the course of
690 the recording session (**Figure 6E**). We then compared such trajectories between central and
691 peripheral recordings from the same day by generating the pupil center location density maps,

JNeurosci Accepted Manuscript

692 which were then statistically compared using the permutation test (see Methods for details). We
693 did not find statistically significant difference in the pair of pupil center location density maps
694 from central and peripheral trials obtained each day for each mouse. To compare across mice in
695 CTL and DF groups for pre and post sessions, we extracted the Pearson correlation coefficient
696 for each pair of pupil center location density maps for central and peripheral trials obtained on
697 the same day for each mouse. There was no statistically significant difference in the pairwise
698 correlation coefficient between CTL and DF groups across pre and post sessions (**Figure 6F**).

699 Together, the pupil diameter data indicate that there were no stimulus-evoked changes
700 in pupil diameter and that it was consistent across various stimulus types and levels, as well as
701 between the pre and post recordings for each experimental condition. The pupil center location
702 data indicate that there is no significant shift in gaze that could have displaced the intended
703 location of our stimulus.

704

705 **Selective enhancement of behavioral detection of static spatial gratings in the peripheral**
706 **visual field following adult-onset deafening**

707 Next, we investigated how DF-induced attenuation of V1 neural activity may affect visual
708 perception. To do this, we trained cohorts of mice (DF: 5 males, 5 females; CTL: 6 males, 5
709 females) on visual detection tasks using well-established operant conditioning techniques. First,
710 adult mice (P50~P70) underwent headplate implantation surgeries, and a group of mice was
711 deafened in the same surgery. Upon recovery, they were water-deprived and habituated to
712 being handled and being head-fixed on the experimental rig. This was followed by a week of
713 detection training, during which we presented the mice with full-field sinusoidal drifting gratings
714 of horizontal orientation, optimal contrast, and optimal spatial frequency, while providing water
715 through a solenoid valve-controlled lick port to establish an association between the stimulus

JNeurosci Accepted Manuscript

and the water reward. Afterward, we presented the mice with the test stimuli (10˚ azimuth wide, full screen height static horizontal orientation gratings with varying spatial frequency or drifting sinusoidal gratings of fixed spatial frequency with varying contrast; see Methods for details) presented either at the central (10-20˚ azimuth) or the peripheral (90-100˚ azimuth) visual field (**Figure 7A**). Mice were required to lick to initiate the water dispensing. By withholding licking and then licking only after the stimulus had been presented, the mouse received the water, which indicated detection of the stimulus (**Figure 7B**). Trials were automatically initiated at a random time drawn from a preset uniform distribution. The range of contrast or spatial frequency levels, selected by the experimenter at the start of the session, was based on the previous day's performance and included a mix of stimuli the mice could detect and newer, more difficult ones. Each mouse performed ~180 trials each day on average, and, for each day, each of the stimulus levels chosen was presented for an equal number of trials. Mice were tested until they reached a ceiling performance in the level of stimulus they could detect, at which point, we calculated their detection rate for each stimulus tested (see Methods for details). The average detection rate for each stimulus during the last 5 sessions was plotted and fitted with the logistic function to calculate the detection threshold, which is the stimulus level at 50% detection rate (**Figure 7C-E**). Above this is considered above-chance performance.

For static gratings with varying spatial frequencies, we observed higher spatial-frequency detection in the central visual field than in the peripheral visual field in control (CTL) mice (**Figure 7C, D**). In adult-onset deaf (DF) mice, the detection of static gratings presented in the central visual field was on par with CTL mice, but there was statistically significant improvement in the detection of stimuli presented in the peripheral visual field with a higher spatial frequency detection threshold (**Figure 7C, D**). In contrast, we did not observe a significant difference in the detection of drifting sinusoidal gratings presented at varying contrast levels between CTL and DF, where both groups showed better detection at lower contrast levels

JNeurosci Accepted Manuscript

741 in the central visual field compared to the periphery (**Figure 7E, F**). We also analyzed the
742 behavioral d-prime (*d'*), another metric often used for determining discrimination of signal from
743 noise. This confirmed significant improvement only in the peripheral spatial acuity for static
744 stimuli (**Supplementary Figure 1**). These results indicate that visual detection is better in the
745 central visual field of mice, and that there is a selective improvement in the spatial acuity of
746 static gratings in the peripheral visual field after adult-onset deafening.

747

JNeurosci Accepted Manuscript

Discussion

Here, we report that adult-onset DF exaggerates the visual stimulus-induced attenuation of neural responses in L2/3 of the mouse V1, with behavioral consequences. Attenuation of responses was observed for spatial frequency-modulated static gratings (**Figure 2**) and contrast-modulated moving gratings (**Figure 4**). DF-induced attenuation was particularly prominent and widespread for stimuli presented in the peripheral visual field. Despite the greater magnitude of response attenuation in the DF group, it minimally affected the accuracy of population responses to decode the visual stimuli presented in the periphery (**Figures 3 and 5**). The response attenuation was not likely due to changes in the arousal state or gaze across days, as assessed by analyzing the pupil changes during sessions (**Figure 6**). Furthermore, adult-onset DF mice showed selective behavioral improvement in visual acuity to static gratings presented in the peripheral visual field without improvement in contrast sensitivity to moving gratings (**Figure 7**). Our results support the view that adult-onset DF may optimize neural processing of visual stimuli in L2/3 V1 by enhancing attenuation to repetitive exposure and specifically improves spatial acuity in the peripheral visual field, which we interpret as cross-modal compensatory plasticity to improve visual function following deafness.

When measuring population responses in V1 L2/3 using 2-photon calcium imaging, we found greater and more widespread attenuation of stimulus-evoked responses, especially in the peripheral visual field, following DF (**Figures 2 and 4**). Attenuation of stimulus-evoked responses in V1 L2/3 following repeated exposure has been reported in normal-sighted mice (Homann et al., 2022; Niraula et al., 2023; Lopez-Ortega et al., 2024), as well as across sensory cortical areas in primates (Grill-Spector et al., 2006). It is thought that this leads to enhanced novelty detection, prevents saturation of the neural response function by increasing its dynamic range, and reduces redundancies in the neural code and metabolic costs, thereby increasing encoding efficacy (Grill-Spector et al., 2006). The proposed underlying neural mechanisms

JNeurosci Accepted Manuscript

include decreased firing rate, sparser responsive neurons due to sharpening of the tuning curves, a shorter latency or shorter duration of activity, or a combination of these three phenomena. The greater attenuation of visually evoked responses seen in V1 L2/3 of DF mice could indicate more efficient visual processing that could improve visual function. Consistent with this, we observed improved behavioral visual acuity in the peripheral visual field (**Figure 7**). Cross-modal compensatory plasticity, which improves functionality of the spared senses, has also been observed in adult A1 after visual deprivation. In this case, it is associated with synaptic plasticity, circuit refinement, and improved high-frequency hearing (Petrus et al., 2014; Meng et al., 2015; Petrus et al., 2015; Meng et al., 2017; Solarana et al., 2019; Jendrichovsky et al., 2024). However, there are some key differences. In adult A1 L2/3, a week of visual deprivation significantly reduced the proportion of stimulus-responsive cells, with some increase in response amplitude at mid-frequency ranges and a relative increase in the fraction of cells responding to higher frequency tones (Solarana et al., 2019). The reduction in auditory responsive neuronal population is likely driven by a homeostatic reduction in the strength of lateral excitatory inputs and potentiation of inhibitory inputs to A1 L2/3 (Petrus et al., 2015), as well as refinement of local circuit connectivity (Meng et al., 2015). In our study, DF did not significantly alter the fraction of visually responsive cells in V1 L2/3 (**Figures 3A and 5A**). This suggests that the mechanisms of compensatory plasticity are likely different across the primary sensory cortices and/or depend on the nature of the deprived sense. Our result showing no significant reduction in the fraction of responsive neurons across days of visual stimuli session in CTL mice is at odds with prior studies showing a reduction in visually responsive neurons after 4-8 days (Niraula et al., 2023; Lopez-Ortega et al., 2024). The apparent discrepancy may be due to daily sessions used for their longitudinal studies and the use of full-field visual stimuli. We intentionally ran 2 daily pre and post sessions each to minimize response attenuation; hence it is possible that with more sessions, we could have seen significant changes in the fraction of responsive neurons even in the CTL. Regardless, our observation that DF

JNeurosci Accepted Manuscript

exaggerates attenuation of responses without significantly decreasing the fraction of responsive neurons suggests that the reduction in response amplitude is a point of regulation for cross-modal compensatory plasticity.

Previous studies reported that compensatory plasticity in the spared sensory cortices involves potentiation of the feedforward inputs (Petrus et al., 2014; Petrus et al., 2015) via Hebbian long-term potentiation (LTP) (Rodriguez et al., 2018) and weakening of lateral intracortical inputs to L2/3 (Goel et al., 2006; He et al., 2012; Petrus et al., 2015). It is thought that potentiation of feedforward inputs increases the synaptic modification threshold, leading to depression of the relatively weak lateral intracortical synapses through homeostatic metaplasticity (Lee, 2023). Mechanistically, this is observed as a widespread downregulation of synaptic AMPA receptors in the spared primary sensory cortices (Goel et al., 2006). Such widespread depression of excitatory synapses together with stronger inhibition in the spared sensory cortex (Petrus et al., 2015) could explain the exaggerated attenuation of V1 L2/3 responses following DF.

Despite the greater attenuation of neural responses to visual stimuli after DF, there was minimal impact on the decoding capability of the neural population (**Figures 3B, C and 5B, C**). The neural responses of V1 L2/3 in DF mice were able to decode the stimulus features presented in the peripheral visual field with decoding accuracy on par with responses recorded before DF, as well as those recorded from CTL mice. This suggests that smaller neural responses due to attenuation do not greatly impact the ability of the network to encode visual features. Furthermore, contrast sensitivity of neurons was also largely unaffected following DF (**Figure 6D, E**). These results are consistent with the idea that there may be more efficient coding of visual features after adult-onset DF. In line with this interpretation, we observed improvement on behaviorally measured visual acuity in the peripheral visual field of DF mice (**Figure 7**). A recent study reported that visuomotor training reduces intermediate neural

JNeurosci Accepted Manuscript

responses, which sparsens V1 population code to orthogonalize stimulus representation and improve behavioral performance (Failor et al., 2025). Non-uniform response attenuation observed after DF **(Figure 2)** may similarly benefit population coding.

While DF enhanced neural attenuation across the 2 types of visual stimuli used in our study, the behavioral gain was selective for the spatial acuity of static gratings only in the peripheral visual field (**Figure 7**). There are several possibilities for this apparent discrepancy. First, the detection of visual stimuli in the central visual field may already be optimal, such that it is not affected by further refinement of V1 circuitry. Similar to humans, mice have higher density photoreceptors in their retina corresponding to the central visual field (Volland et al., 2015). Second, while V1 L2/3 responds to contrast-modulated moving gratings, it may not be the circuit responsible for mediating behavioral detection of such stimuli. Detection of some visual stimuli can bypass V1 by utilizing subcortical circuits (Leh et al., 2010; Kinoshita et al., 2019), including the superior colliculus, which in mice has its own map of motion directions (Li et al., 2020) and can mediate contrast detection when V1 is inactivated (Cone et al., 2024). Such a subcortical circuit has been proposed to serve, at least in part, what is termed “blindsight,” which refers to residual visual abilities seen after V1 lesions (Sanders et al., 1974; Leh et al., 2010; Kinoshita et al., 2019). Third, there is evidence that easier sensory tasks do not require the primary sensory cortices (Hong et al., 2018; Ceballo et al., 2019). Furthermore, there is evidence that even when A1 is necessary for learning to discriminate simple tones, it becomes dispensable once the mice become experts (Drieu et al., 2025). We noticed that the contrast-modulated moving grating task was easier for mice to learn than the spatial acuity task, as determined by requiring fewer training sessions to reach plateau performance (median session number: static central = 24, static peripheral = 33; moving central = 5, moving peripheral = 8). Regardless, our results suggest that improvement in visual function at the behavioral detection level is limited to the peripheral visual field and specific to the spatial acuity of static stimuli. The selective

JNeurosci Accepted Manuscript

849 improvement in visual performance in the peripheral visual field has been documented in
850 congenitally deaf human subjects, which has been attributed to increased visual attention in the
851 periphery (Neville and Lawson, 1987; Loke and Song, 1991; Bavelier et al., 2000; Proksch and
852 Bavelier, 2002). While our effect could also be due to selective visual attention, at least it is not
853 likely due to changes in gaze-directed attention or general arousal as we did not see consistent
854 changes in gaze or pupil size (**Figure 6**).

855 In summary, our findings suggest neural response attenuation to visual stimuli as a
856 potential mechanism for cross-modal compensatory adaptation in adult V1, which may benefit
857 visual detection of select features in the periphery.

JNeurosci Accepted Manuscript

References

Barkat TR, Polley DB, Hensch TK (2011) A critical period for auditory thalamocortical connectivity. Nature Neurosci 14:1189-1194.

Bavelier D, Dye MW, Hauser PC (2006) Do deaf individuals see better? Trends Cogn Sci 10:512-518.

Bavelier D, Tomann A, Hutton C, Mitchell T, Corina D, Liu G, Neville H (2000) Visual attention to the periphery is enhanced in congenitally deaf individuals. J Neurosci 20:RC93.

Bedny M, Pascual-Leone A, Dodell-Feder D, Fedorenko E, Saxe R (2011) Language processing in the occipital cortex of congenitally blind adults. Proc Natl Acad Sci USA 108:4429-4434.

Brainard DH (1997) The Psychophysics Toolbox. Spat Vis 10:433-436.

Buchel C, Price C, Frackowiak RS, Friston K (1998) Different activation patterns in the visual cortex of late and congenitally blind subjects. Brain 121 (Pt 3):409-419.

Burton H, Snyder AZ, Conturo TE, Akbudak E, Ollinger JM, Raichle ME (2002) Adaptive changes in early and late blind: a fMRI study of Braille reading. J Neurophysiol 87:589-607.

Camillo D, Ahmadlou M, Heimel JA (2020) Contrast-Dependence of Temporal Frequency Tuning in Mouse V1. Front Neurosci 14:868.

Cang J, Fu J, Tanabe S (2023) Neural circuits for binocular vision: Ocular dominance, interocular matching, and disparity selectivity. Front Neural Circuits 17:1084027.

Ceballo S, Piwkowska Z, Bourg J, Daret A, Bathellier B (2019) Targeted Cortical Manipulation of Auditory Perception. Neuron 104:1168-1179 e1165.

Cone JJ, Mitchell AO, Parker RK, Maunsell JHR (2024) Stimulus-dependent differences in cortical versus subcortical contributions to visual detection in mice. Curr Biol 34:1940-1952 e1945.

Drieu C, Zhu Z, Wang Z, Fuller K, Wang A, Elnozahy S, Kuchibhotla K (2025) Rapid emergence of latent knowledge in the sensory cortex drives learning. Nature 641:960-970.

Durand S, Iyer R, Mizuseki K, de Vries S, Mihalas S, Reid RC (2016) A Comparison of Visual Response Properties in the Lateral Geniculate Nucleus and Primary Visual Cortex of Awake and Anesthetized Mice. J Neurosci 36:12144-12156.

Ewall G, Parkins S, Lin A, Jaoui Y, Lee H-K (2021) Cortical and subcortical circuits for cross-modal plasticity induced by loss of vision. Front Neural Circuits 15:665009.

Failor SW, Carandini M, Harris KD (2025) Visual experience orthogonalizes visual cortical stimulus responses via population code transformation. Cell Rep 44:115235.

Goel A, Jiang B, Xu LW, Song L, Kirkwood A, Lee HK (2006) Cross-modal regulation of synaptic AMPA receptors in primary sensory cortices by visual experience. Nature Neurosci 9:1001-1003.

JNeurosci Accepted Manuscript

Grill-Spector K, Henson R, Martin A (2006) Repetition and the brain: neural models of stimulus-specific effects. Trends Cogn Sci 10:14-23.

He K, Petrus E, Gammon N, Lee HK (2012) Distinct sensory requirements for unimodal and cross-modal homeostatic synaptic plasticity. J Neurosci 32:8469-8474.

Histed MH, Carvalho LA, Maunsell JH (2012) Psychophysical measurement of contrast sensitivity in the behaving mouse. J Neurophysiol 107:758-765.

Homann J, Koay SA, Chen KS, Tank DW, Berry MJ, 2nd (2022) Novel stimuli evoke excess activity in the mouse primary visual cortex. Proc Natl Acad Sci USA 119:e2108882119.

Hong YK, Lacefield CO, Rodgers CC, Bruno RM (2018) Sensation, movement and learning in the absence of barrel cortex. Nature 561:542-546.

Hoy JL, Niell CM (2015) Layer-specific refinement of visual cortex function after eye opening in the awake mouse. J Neurosci 35:3370-3383.

Huber E, Chang K, Alvarez I, Hundle A, Bridge H, Fine I (2019) Early Blindness Shapes Cortical Representations of Auditory Frequency within Auditory Cortex. J Neurosci 39:5143-5152.

Jendrichovsky P, Lee HK, Kanold PO (2024) Brief periods of visual deprivation in adults increase performance on auditory tasks. iScience 27:110936.

Juavinett AL, Nauhaus I, Garrett ME, Zhuang J, Callaway EM (2017) Automated identification of mouse visual areas with intrinsic signal imaging. Nature Prot 12:32-43.

Kinoshita M, Kato R, Isa K, Kobayashi K, Kobayashi K, Onoe H, Isa T (2019) Dissecting the circuit for blindsight to reveal the critical role of pulvinar and superior colliculus. Nature Comm 10:135.

Kral A, Sharma A (2023) Crossmodal plasticity in hearing loss. Trends Neurosci 46:377-393.

Lapanja T, Micheli P, Gonzalez-Guerra A, Radomskyi O, De Franceschi G, Muraveva A, Attinger A, Roth CN, Tripodi M, Boissonnet T, Sabbadini M, Juttner J, Ala-Laurila P, Keller G, Allina GP, Asari H, Rompani SB (2025) Pupil size modulation drives retinal activity in mice and shapes human perception. Nature Comm 16:7334.

Larsen RS, Waters J (2018) Neuromodulatory Correlates of Pupil Dilation. Front Neural Circuits 12:21.

Lee H-K (2023) Metaplasticity framework for cross-modal synaptic plasticity in adults. Frontiers Synaptic Neurosci 14:1087042.

Leh SE, Ptito A, Schonwiesner M, Chakravarty MM, Mullen KT (2010) Blindsight mediated by an S-cone-independent collicular pathway: an fMRI study in hemispherectomized subjects. J Cogn Neurosci 22:670-682.

Li YT, Turan Z, Meister M (2020) Functional Architecture of Motion Direction in the Mouse Superior Colliculus. Current Biol 30:3304-3315 e3304.

Loke WH, Song SR (1991) Central and Peripheral Visual Processing in Hearing and Nonhearing Individuals. B Psychonomic Soc 29:437-440.

JNeurosci Accepted Manuscript

933 Lopez-Ortega E, Choi JY, Hong I, Roth RH, Cudmore RH, Huganir RL (2024) Stimulus-
934 dependent synaptic plasticity underlies neuronal circuitry refinement in the mouse
935 primary visual cortex. Cell Rep 43:113966.

936 Mathis A, Mamidanna P, Cury KM, Abe T, Murthy VN, Mathis MW, Bethge M (2018)
937 DeepLabCut: markerless pose estimation of user-defined body parts with deep learning.
938 Nature Neurosci 21:1281-1289.

939 Meng X, Kao JP, Lee HK, Kanold PO (2015) Visual Deprivation Causes Refinement of
940 Intracortical Circuits in the Auditory Cortex. Cell Rep 12:955-964.

941 Meng X, Kao JP, Lee HK, Kanold PO (2017) Intracortical Circuits in Thalamorecipient Layers of
942 Auditory Cortex Refine after Visual Deprivation. eNeuro 4(2):ENEURO.0092-17.2017 1-
943 11.

944 Mesik L, Lee H-K (2023) Cross-modal plasticity of cortical and thalamic circuits. In: The cerebral
945 cortex and thalamus (Usrey WM, Sherman SM, eds), pp 573-582. New York, U. S. A.:
946 Oxford University Press.

947 Meyer AF, O'Keefe J, Poort J (2020) Two Distinct Types of Eye-Head Coupling in Freely Moving
948 Mice. Current Biol 30:2116-2130 e2116.

949 Meyers EM (2013) The neural decoding toolbox. Front Neuroinform 7:8.

950 Neske GT, Nestvogel D, Steffan PJ, McCormick DA (2019) Distinct Waking States for Strong
951 Evoked Responses in Primary Visual Cortex and Optimal Visual Detection Performance.
952 J Neurosci 39:10044-10059.

953 Neville HJ, Lawson D (1987) Attention to central and peripheral visual space in a movement
954 detection task: an event-related potential and behavioral study. II. Congenitally deaf
955 adults. Brain Res 405:268-283.

956 Niell CM, Stryker MP (2008) Highly selective receptive fields in mouse visual cortex. The J
957 Neurosci 28:7520-7536.

958 Niraula S, Hauser WL, Rouse AG, Subramanian J (2023) Repeated passive visual experience
959 modulates spontaneous and non-familiar stimuli-evoked neural activity. Sci Rep
960 13:20907.

961 Pachitariu M, Stringer C, Schröder S, Dipoppa M, Rossi LF, Carandini M, Harris KD (2016)
962 Suite2p: beyond 10,000 neurons with standard two-photon microscopy. BioRxiv 061507.

963 Parker PRL, Abe ETT, Leonard ESP, Martins DM, Niell CM (2022) Joint coding of visual input
964 and eye/head position in V1 of freely moving mice. Neuron 110:3897-3906 e3895.

965 Petrus E, Rodriguez G, Patterson R, Connor B, Kanold PO, Lee HK (2015) Vision Loss Shifts
966 the Balance of Feedforward and Intracortical Circuits in Opposite Directions in Mouse
967 Primary Auditory and Visual Cortices. J Neurosci 35:8790-8801.

968 Petrus E, Isaiah A, Jones AP, Li D, Wang H, Lee HK, Kanold PO (2014) Crossmodal induction
969 of thalamocortical potentiation leads to enhanced information processing in the auditory
970 cortex. Neuron 81:664-673.

JNeurosci Accepted Manuscript

971 Privitera M, Ferrari KD, von Ziegler LM, Sturman O, Duss SN, Floriou-Servou A, Germain PL,
972 Vermeiren Y, Wyss MT, De Deyn PP, Weber B, Bohacek J (2020) A complete
973 pupillometry toolbox for real-time monitoring of locus coeruleus activity in rodents.
974 Nature Prot 15:2301-2320.

975 Proksch J, Bavelier D (2002) Changes in the spatial distribution of visual attention after early
976 deafness. J Cogn Neurosci 14:687-701.

977 Rochefort NL, Narushima M, Grienberger C, Marandi N, Hill DN, Konnerth A (2011)
978 Development of direction selectivity in mouse cortical neurons. Neuron 71:425-432.

979 Rodriguez G, Chakraborty D, Schrode KM, Saha R, Uribe I, Lauer AM, Lee HK (2018) Cross-
980 Modal Reinstatement of Thalamocortical Plasticity Accelerates Ocular Dominance
981 Plasticity in Adult Mice. Cell Rep 24:3433-3440 e3434.

982 Sadato N, Pascual-Leone A, Grafman J, Ibanez V, Deiber MP, Dold G, Hallett M (1996)
983 Activation of the primary visual cortex by Braille reading in blind subjects. Nature
984 380:526-528.

985 Sanders MD, Warrington EK, Marshall J, Wieskrantz L (1974) "Blindsight": Vision in a field
986 defect. Lancet 1:707-708.

987 Schuett S, Bonhoeffer T, Hubener M (2002) Mapping retinotopic structure in mouse visual
988 cortex with optical imaging. J Neurosci 22:6549-6559.

989 Solarana K, Liu J, Bowen Z, Lee HK, Kanold PO (2019) Temporary Visual Deprivation Causes
990 Decorrelation of Spatiotemporal Population Responses in Adult Mouse Auditory Cortex.
991 eNeuro 6(6):ENEURO.0269-19.2029 1-13.

992 Viglione A, Mazziotti R, Pizzorusso T (2023) From pupil to the brain: New insights for studying
993 cortical plasticity through pupillometry. Front Neural Circuits 17:1151847.

994 Vinck M, Batista-Brito R, Knoblich U, Cardin JA (2015) Arousal and locomotion make distinct
995 contributions to cortical activity patterns and visual encoding. Neuron 86:740-754.

996 Volland S, Esteve-Rudd J, Hoo J, Yee C, Williams DS (2015) A comparison of some
997 organizational characteristics of the mouse central retina and the human macula. PloS
998 One 10:e0125631.

999 Wobbrock JO, Findlater L, Gergle D, Higgins JJ (2011) The aligned rank transform for
1000 nonparametric factorial analyses using only ANOVA procedures. In: Proceedings of the
1001 SIGCHI Conference on Human Factors in Computing Systems (CHI ‘ 11), pp 143-146.
1002 New York: ACM Press.

1003 Zhang X, An X, Liu H, Peng J, Cai S, Wang W, Lin DT, Yang Y (2015) The topographical
1004 arrangement of cutoff spatial frequencies across lower and upper visual fields in mouse
1005 V1. Sci Rep 5:7734.

1006 Zhu S, Bao X, Lomber SG (2026) Time course of visual plasticity following adult-onset
1007 deafness. Sci Rep 16:9384.

1008

JNeurosci Accepted Manuscript

1009

1010

JNeurosci Accepted Manuscript

Figure Legends

Figure 1. Schematic of 2-photon calcium imaging of the visual cortex of adult-onset deaf mice.

(A) Schematic diagram of the experimental setup and timeline of the experiment procedure starting with GCamp8s injections in V1 at ~P60. CTL mice followed the same timeline without being deafened at P92. The upper left panel includes the range of binocular visual field, which spans about 40˚ in the central visual field, and the monocular visual field spanning laterally around the mouse's head (Cang et al., 2023). A schematic of the recording setup is shown on the right, with the mice sitting head-fixed on a cradle, the stimulus screen positioned in front of their right eye, and the pupil camera positioned in front of their left eye. The circle inset shows the position of the stimulus screen relative to the mouse, being 30 cm from the right pupil, and angled so that the central stimulus spans 0˚-10˚ azimuth, which is within the binocular visual field, and the peripheral stimulus spans 80˚-90˚ azimuth in the monocular visual field. The height of the screen was positioned so that its midpoint directly lines up with the pupil. Some of the images used in the schematics are from Zenodo (https://zenodo.org/records/3925903), SciDraw (https://scidraw.io/drawing/183), and Servier Medical Art (https://smart.servier.com/smart_image/syringe/) licensed under CC BY 4.0 (https://creativecommons.org/licenses/by/4.0/).

(B) Sample immunofluorescence images of mouse cochlear hair cells stained with Alexa Fluor™ 488 phalloidin (green) and counterstained with DAPI (blue). In all images, three layers of outer hair cells are visible on top of one layer of inner hair cells. Across the entire basilar membrane structure, DF mice show substantially less phalloidin fluorescent signal compared to CTL mice, which indicate damage to the hair cells.

JNeurosci Accepted Manuscript

(C) Intrinsic signal imaging (ISI) map of V1 and higher order visual areas overlaying an image of vasculature. V1 is outlined with a white dashed line. The network of the vasculature is used to guide locations of 2-photon imaging fields to the lateral V1 representing the central visual field and the medial V1 representing the peripheral visual field. The contour of the circular cranial window is visible near the edges of the image. (Coordinates: A = anterior; P = posterior; M = medial; L = lateral).

(D) Example image of a 2-photon imaging field of view extracted from Suite2P's user interface. Fluorescent neuronal soma are visible as bright dots scattered around the dark vasculature. Regions of interest (ROIs) identified by the Suite2p image processing session were randomly colored as shown.

(E) Example traces from four imaging sessions of two mice, one CTL (left panel) and one DF (right panel). The sequence of stimulus presentation is shown at the top as color coded vertical lines. For this example, recordings from sessions using acuity stimulus of varying spatial frequency were selected (bkg: isoluminance background, 0.1 cpd, 0.3 cpd, 0.5 cpd, 0.7 cpd, 0.9 cpd, and 1.1 cpd static sinusoidal gratings of horizontal orientation; see inset for color codes). Contrast stimuli consisted of 4%, 8%, 16%, 32%, 64%, and 85% contrast sinusoidal gratings of horizontal orientation drifting downwards. Contrast-stimulus sessions follow the same color-pattern sequence, which similarly labeled the stimuli from smallest to the largest percentage contrast. In this example, each trace corresponds to responses recorded from an ROI in one session. Responses from randomly selected 14 ROIs from a pre recording session are shown in black, and another set of 14 ROIs from a post recording session are shown in maroon.

Figure 2. Adult-onset deafness results in more attenuation of acuity stimulus-evoked responses in L2/3 of V1

JNeurosci Accepted Manuscript

(A) Per-trial averaged $\Delta F/F_0$ traces of control (left panel) and deaf (right panel) mice recorded from lateral V1 upon presentation of acuity stimuli (background to 0.7 cpd) in the central visual field (top traces) and medial V1 with presentation in the peripheral visual field (bottom traces). Only ROIs with significant responses to at least one visual stimulus were included in the analysis. While the same area of V1 was targeted for recording across days in each mouse, the same set of cells was not longitudinally tracked. For each stimulus condition, the post-session traces recorded 1 week after the pre-session are shown in orange and are plotted over the pre-session traces in green. The duration of the stimulus presentation (300 ms) is shaded in light gray. (DF-Central: 5 mice; DF-Peripheral: 6 mice; CTL-Central: 5 mice; CTL-Peripheral: 6 mice).

(B) Heatmaps of the post-stimulus onset peak response of every stimulus-responsive cell for each experimental condition. Responses with $\Delta F/F_0$ equal to or larger than 2.5 were collapsed into a single-color group.

(C and D) Mean ± SEM of stimulus-evoked responses for each stimulus condition. In (C), post-stimulus onset peak values of the $\Delta F/F_0$ traces were averaged (CTL-Central: $F(6, 3{,}874) = 0.9161$, $p = 0.482$; CTL-Peripheral: $F(6, 7{,}415) = 3.4828$, $p = 0.0019$; DF-Central: $F(6, 5{,}470) = 3.9755$, $p = 0.0006$; DF-Peripheral: $F(6, 4{,}818) = 8.2463$, $p = 6.6569e^{-09}$, ART 2-way ANOVA). Effect size (r) for peak: CTL-Peripheral: 0.5 cpd = 0.385, 0.7 cpd = 0.642; DF-Central: 0.7 cpd = 0.663, 1.1 cpd = 0.0603; DF-Peripheral peak: bkg = 0.385, 0.3 cpd = 0.899, 0.5 cpd = 0.385.

In (D), the area under the curve (AUC) of $\Delta F/F_0$ trace between the start of stimulus onset to 2 s afterward was quantified and averaged (CTL-Central: $F(6, 3{,}874) = 1.8063$, $p = 0.0938$; CTL-Peripheral: $F(6, 7{,}415) = 6.9384$, $p = 2.2817e^{-07}$; DF-Central: $F(6, 5{,}470) = 4.7047$, $p = 8.7428e^{-05}$; DF-Peripheral: $F(6, 4{,}818) = 14.5208$, $p = 1.7070e^{-16}$, ART 2-way ANOVA). Post hoc multigroup comparisons: *p < 0.05, **p<0.01; ***p< 0.005. Effect size (r) for AUC: CTL-Peripheral: 0.5 cpd = 0.128, 0.9 cpd = 0.128; DF-Central: 0.5 cpd = 0.181, 0.7cpd = 0.784; DF-Peripheral peak: 0.3 cpd = 0.813, 0.5 cpd = 0.556.

Neurosci Accepted Manuscript

Figure 3. Responsive cell proportion and decoding capability of acuity stimulus-evoked responses remain comparable in deafened mice

(A) Left: The total number of cells in each image plane with sufficient GCaMP fluorescence to be detectable by the Suite2p algorithm as an ROI. Data from the central and peripheral recordings within the experimental condition CTL/DF were grouped together for plotting [F(1, 150.4351) = 0.0162, p = 0.8988, ART 2-way ANOVA]. Middle: The number of responsive cells in each image plane defined as ROIs with statistically significant responses to at least one stimulus [F(1, 150.307) = 1.5167, p = 0.22, ART 2-way ANOVA]. Right: The proportion of responsive cells in each image plane calculated as the number of responsive cells divided by the number of total cells detected [F(1, 150.5892) = 1.9986, p = 0.1595, ART 2-way ANOVA].

(B) Per-trial traces of decoding accuracy of the 0.3 cpd stimulus versus the isoluminance background in the peripheral visual field. Traces are the average of all traces within the same experimental condition (black line) ± SEM (dark gray shade). Stimulus onset is at 0 indicated by the vertical dotted line, and lasted for 300 ms, shown as a light gray shaded vertical bar. *d'* values for peak decoding accuracy: 0.3 cpd CTL pre = 3.2685, 0.3 cpd CTL post = 4.2272, 0.5 cpd CTL pre = 2.3582, 0.5 cpd CTL post = 3.0085; 0.3 cpd DF pre = 3.1928, 0.3 cpd DF post = 2.7393, 0.5 cpd DF pre = 1.6751, 0.5 cpd DF post = 2.25673.

(C) Top panels: Averages of stimulus-evoked peak decoding accuracy for the 0.3 cpd stimulus [left, F(1, 75.38) = 0.9172, p = 0.3413, ART 2-way ANOVA] and the 0.5 cpd stimulus [right, F(1, 75.71) = 1.1826, p = 0.2803, ART 2-way ANOVA], plotted as mean ± SEM. Bottom panels: Integrated accuracy computed as the area under the decoding accuracy curve above 50% chance level for the 2 s post-stimulus onset duration. Data are similarly plotted as mean ± SEM

JNeurosci Accepted Manuscript

for the 0.3 cpd stimulus [left, F(1, 75.32) = 1.9317, p = 0.1687, ART 2-way ANOVA] and the 0.5 cpd stimulus [right, F(1, 75.48) = 1.6223, p = 0.2067, ART 2-way ANOVA].

Figure 4. Adult-onset deafness causes more attenuation of contrast stimulus-evoked responses in L2/3 of V1

(A) Per-trial averaged $\Delta F/F_0$ of control (left panel) and deaf (right panel) mice recorded from lateral V1 upon presentation of contrast modulated drifting grating stimuli (background to 32% contrast) in the central visual field (top traces) and medial V1 with presentation in the peripheral visual field (bottom traces). For each stimulus condition, the post-session traces are shown in red and are plotted over the pre-session traces in blue. The duration of the stimulus presentation (1.3 s) is shown as light gray shaded vertical bar. (DF-Central: 5 mice; DF-Peripheral: 5 mice; CTL-Central: 5 mice; CTL-Peripheral: 5 mice).

(B) Heatmaps of the post-stimulus onset peak response of every stimulus-responsive ROI for each experimental condition. Responses with $\Delta F/F_0$ equal to or larger than 2.5 were collapsed into a single-color group.

(C and D) Mean ± SEM stimulus-evoked responses for each stimulus condition. In (C), average post-stimulus onset peak values of the $\Delta F/F_0$ traces are graphed for each contrast level [CTL-Central: F(6, 6982) = 1.7653, p = 0.1020; CTL-Peripheral: F(6, 5988) = 2.1652, p = 0.0433; DF-Central: F(6, 6513) = 3.8918, p = 0.0007; DF-Peripheral: F(6, 4644) = 3.1846, p = 0.0040, ART 2-way ANOVA). Effect size (r) for peak: CTL-Peripheral: 85% = 0.543; DF-Central: 8% = 0.0603, 16% = 0.181; DF-Peripheral: 8% = 0.905, 16% = 0.905, 64% = 0.784. In (D), the AUC of $\Delta F/F_0$ traces between the start of stimulus onset and 3 s afterward was quantified and averaged for each contrast level [CTL-Central: F(6, 6982) = 2.6444, p = 0.0146; CTL-Peripheral: F(6, 5988) = 5.8632, p = 4.1437e-06; DF-Central: F(6, 6513) = 6.1822, p = 1.7613e-06; DF-

JNeurosci Accepted Manuscript

Peripheral: F(6, 4644) = 3.3264, p = 0.0029, ART 2-way ANOVA]. Post hoc multigroup comparisons: *p < 0.05, **p < 0.01; ***p < 0.005. Effect size (r) for AUC: CTL-Central: 16% = 0.302; CTL-Peripheral: 85% = 0.422; DF-Central: 8% = 0.181, 16% = 0.181, 85% = 0.181; DF-Peripheral: 8% = 0.302, 16% = 0.905, 64% = 0.0603.

Figure 5. Responsive cell proportion, decoding capability, and contrast sensitivity of contrast stimulus-evoked responses remain comparable in deafened mice

(A) Left: The total number of cells in image plane with sufficient GCaMP fluorescence to be detectable by the Suite2p algorithm as an ROI. Data from the central and peripheral recordings within the experimental condition CTL/DF were grouped together for plotting [F(1, 128.0934) = 0.1194, p = 0.7302, ART 2-way ANOVA] . Middle: The number of responsive cells in each image plane as defined as ROIs with statistically significant responses to at least one stimulus [F(1, 128.222) = 0.3195, p = 0.573, ART 2-way ANOVA] . Right: The proportion of responsive cells in each imaged plane calculated as the number of responsive cells divided by the number of total cells [F(1, 128.6753) = 1.6545, p = 0.2007, ART 2-way ANOVA].

(B) Per-trial traces of decoding accuracy of the16% contrast stimulus versus the isoluminance background in the peripheral visual field. Traces are the average of all traces within the same experimental condition (black line) ± SEM (dark gray shade). Stimulus onset is at 0 indicated by a vertical dotted line and lasted for 1.3 s (light gray shaded vertical bar). *d'*-values for peak decoding accuracy: 8% CTL pre = 3.0645, 8% CTL post =2.6601, 16% CTL pre = 2.0933, 16% CTL post = 2.6293, 64% CTL pre = 2.9242, 64% CTL post = 3.4617; 8% DF pre = 3.0122, 8% DF post = 2.7265, 16% DF pre = 3.5072, 16% DF post = 2.9269, 64% DF pre = 4.0819, 64% DF post = 2.8654.

JNeurosci Accepted Manuscript

(C) Top panels: Mean ± SEM of stimulus-evoked peak decoding accuracy for contrast stimuli displayed at 8% [F(1, 54.2105) = 1.0327, p = 0.3140, ART 2-way ANOVA], 16% [F(1, 54.5398) = 0.6059, p = 0.4397, ART 2-way ANOVA], and 64% [F(1, 53.761) = 1.4316, p = 0.2368, ART 2-way ANOVA] are plotted in each graph. Bottom panels: Integrated accuracy computed as the area under the decoding accuracy curve above 50% chance level for the 3 s post-stimulus onset. Mean ± SEM for contrast stimuli at 8% [F(1, 54.5398) = 0.4614, p = 0.5, ART 2-way ANOVA], 16% [F(1, 54.3355) = 2.4854, p = 0.1207, ART 2-way ANOVA], and 64% [F(1, 54.5398) = 0.5333, p = 0.4684, ART 2-way ANOVA] are plotted in each graph.

(D) Stimulus-evoked responses fitted over the entire range of contrast levels. Top panels: Fitting performed using the peak of post-stimulus onset responses of each cell. The fits of each cell of the same experimental condition (CTL/DF) and recording location (Central/Peripheral) were averaged together. Bottom panels: Similar to top panels except that fitting was performed using the AUC between stimulus onset to 3 s post-onset.

(E) Top panels: The contrast level at which the $\Delta F/F_0$ reached half of its maximum value (C50) for each cell. Data were averaged within each experimental condition and stimulus location and plotted as mean ± SEM [Central: F(1, 529.3477) = 0.416, p = 0.5192; Peripheral: F(1, 443.559) = 0.0002, p = 0.9895, ART 2-way ANOVA]. Bottom panels: The slope of the rising phase of each fit, averaged within each experimental condition and stimulus location and plotted as mean ± SEM [Central: F(1, 529.9739) = 1.4136, p = 0.235; Peripheral: F(1, 446.7834) = 0.2591, p = 0.611, ART 2-way ANOVA].

Figure 6. Pupil size and location are unaffected by stimulus

(A) An example video frame image of the labeling of anterior, posterior, top, and bottom locations on a pupil boundary in DeepLabCut.

JNeurosci Accepted Manuscript

(B) Per-trial changes in pupil diameter aligned to stimulus onset (indicated as dotted vertical line at 0 s in each graph) from an example control mouse (left panels) and an example adult-onset deaf mouse (right panels) during an acuity-stimuli session. Data were normalized to the maximum pupil diameter of the same recording session. Each recording session is plotted individually in the background as light gray lines, their average is plotted in the foreground in black.

(C) Pupil size recorded during experiments using acuity stimuli, normalized to the average pupil size during the background trials of the same recording session. Data were averaged within the same stimulus type and location [CTL-Central: $F(5, 1844) = 0.2198$, $p = 0.9541$; CTL-Peripheral: $F(5, 2142) = 0.2137$, $p = 0.9568$; DF-Central: $F(5, 2168) = 1.8316$, $p = 0.1034$; DF-Peripheral: $F(5, 2704) = 1.8844$, $p = 0.0938$, LME 2-way ANOVA].

(D) Pupil size recorded during experiments using contrast stimuli, normalized to the average pupil size during the background trials of the same recording session. Data were averaged within the same stimulus type and location [CTL-Central: $F(5, 1306) = 0.286$, $p = 0.9212$; CTL-Peripheral: $F(5, 1186) = 1.16$, $p = 0.3262$; DF-Central: $F(5, 1366) = 1.010$, $p = 0.4103$; DF-Peripheral:$F(5, 1785) = 0.141$, $p = 0.9826$, LME 2-way ANOVA].

(E) Example plots of changes in pupil center location throughout a recording session. Pupil center locations tracked during session 1 and 2 (leftmost 2 panels) for central stimuli presentation (top) and peripheral stimuli presentation (bottom). Anterior-posterior coordinates and top-down coordinates of the pupil center at each time frame are plotted in 2D space and connected to the next time frame location with a line. These frame-by-frame pupil center coordinates were fitted with a kernel density to obtain an average density map (third panel from the left; top: central, bottom: peripheral). For the example pair of pupil location density maps, the Pearson correlation coefficient was 0.72, indicating strong correlation. This suggests that on average the spatial drift in the mouse's gaze is quite similar for the central and peripheral trials.

Neurosci Accepted Manuscript

This is confirmed statistically using the permutation test on the average density map of pupil location for central versus peripheral stimuli presentations [Root Mean Square Error (RMSE) = 3.022, Observed Mean Difference = -0.008, Observed Mean Absolute Difference = 0.8821, Permutation Threshold (α = 0.05) = 36.369] and evident from the differential density map (rightmost panel). For all pairs of pupil location density maps examined, the Observed Mean Difference and the Observed Mean Absolute Difference values were all less than the Permutation Threshold.

(F) Across group comparison of the Pearson correlation coefficients of pairwise pupil location density maps of central and peripheral trials obtained on the same day for each mouse. There was no statistically significant interaction between the group (CTL vs. DF) and time (pre vs. post) for acuity experiments [top graph: $F(1,30.3) = 0.1701$, $p = 0.683$, ART 2-way ANOVA] or the contrast experiments [bottom graph: $F(1,12.2) = 0.1366$, $p = 0.718$, ART 2-way ANOVA]. Colored circles indicate the Pearson correlation coefficient values for each pair of density maps with median ± IQR in the foreground.

Figure 7. Adult-onset deafening selectively improves visual acuity in the peripheral visual field

(A) Timeline of the visual detection experiment, starting with the headplate implantation surgery and ototoxic lesioning of DF mice at ~P60. After recovery and habituation, the mice are head-fixed in a cradle, with the visual stimulus screen placed in front of their left eye and positioned such that the central stimulus spans 10-20˚ azimuth (within the binocular visual field) and the peripheral stimulus spans 90-100˚ azimuth (in the monocular visual field) as depicted in the circle inset on the top left. Schematics of the stimuli set used are show on the top right side. For mice that underwent both contrast sensitivity and acuity threshold measurements, contrast

JNeurosci Accepted Manuscript

sensitivity was measured first. Nine mice underwent acuity threshold measurement only, 3 mice underwent contrast sensitivity measurement only, and 9 mice underwent both measurements. The mouse head image in the inset is from SciDraw (https://scidraw.io/drawing/183) licensed under CC BY 4.0.

(B) Example raster plot of the mice's licking behavior throughout a session where a mix of stimuli of varying cpd (left) or varying contrast level (right) was presented. The rate of licks within the background (Bkg)-only window 1 s before stimulus onset (blue shaded area) was quantified and subtracted from the rate of licks within the 1 s post-stimulus onset response (Res) time window (red shaded area) to calculate the detection rate (see Methods for details).

(C) Average detection rates of CTL and a DF groups are plotted as a function of spatial frequencies of static gratings presented in the central (left) and peripheral (right) visual fields. Detection rate of 0.5, which denotes chance level performance and indicates the detection threshold, is denoted as a horizontal dotted line on each graph.

(D) Detection threshold is determined for each mouse as the cpd at which the detection rate is 0.5. The detection thresholds are grouped here by experimental group and stimulus location. Statistical comparison using 2-way ANOVA: interaction between visual field (Central/Peripheral) and experimental condition (CTL/DF): $F(1,16) = 5.255$, $p = 0.0358$, effect of visual field: $F(1,16) = 66.28$, $p < 0.0001$, effect of experimental condition: $F(1,16) = 2.867$, $p = 0.0198$. Post hoc pair-wise comparison (Fisher's LSD) p-values are indicated on the graph. Effect size of the difference in detection threshold between CTL and DF for the peripheral visual field is considered very large (Cohen's $d = 1.44$). Individual colored circles indicate the detection threshold of each mouse. Mean ± SEM are shown in the foreground.

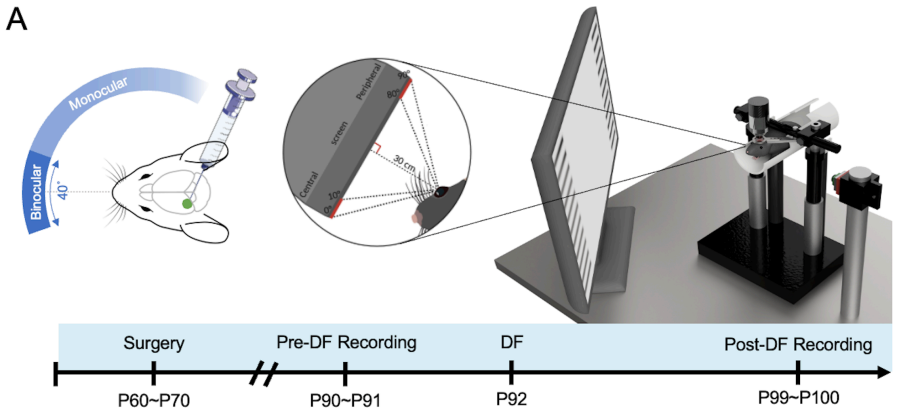
(E) Average detection rate of CTL and DF groups are plotted as a function of contrast levels of drifting gratings presented in the central (left) and peripheral (right) visual fields. A detection rate

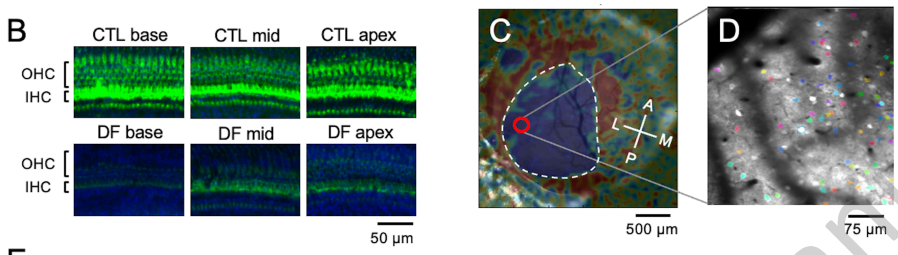
Neurosci Accepted Manuscript

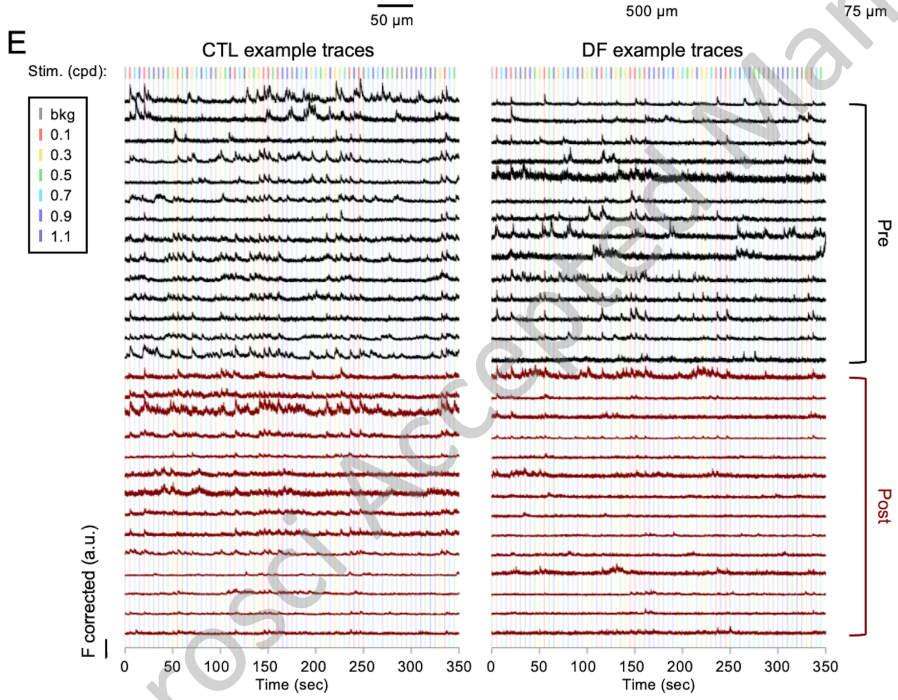
of 0.5, which denotes chance level performance and indicates the detection threshold, is shown as a horizontal dotted line on each graph.

(F) Detection threshold is determined for each mouse as the contrast percentage at which the detection rate is 0.5. The detection thresholds are grouped here by experimental group and stimulus location. Statistical comparison using 2-way ANOVA: interaction between visual field (Central/Peripheral) and experimental condition (CTL/DF): $F(1,10) = 0.4722$, $p = 0.5076$, effect of visual field: $F(1,10) = 18.68$, $p = 0.0015$, effect of experimental condition: $F(1,10) = 0.1129$, $p = 0.7438$. Post hoc pair-wise comparison (Fisher's LSD) p-values are noted on the graph. Individual colored circles indicate the detection threshold of each mouse. Mean ± SEM are shown in the foreground.

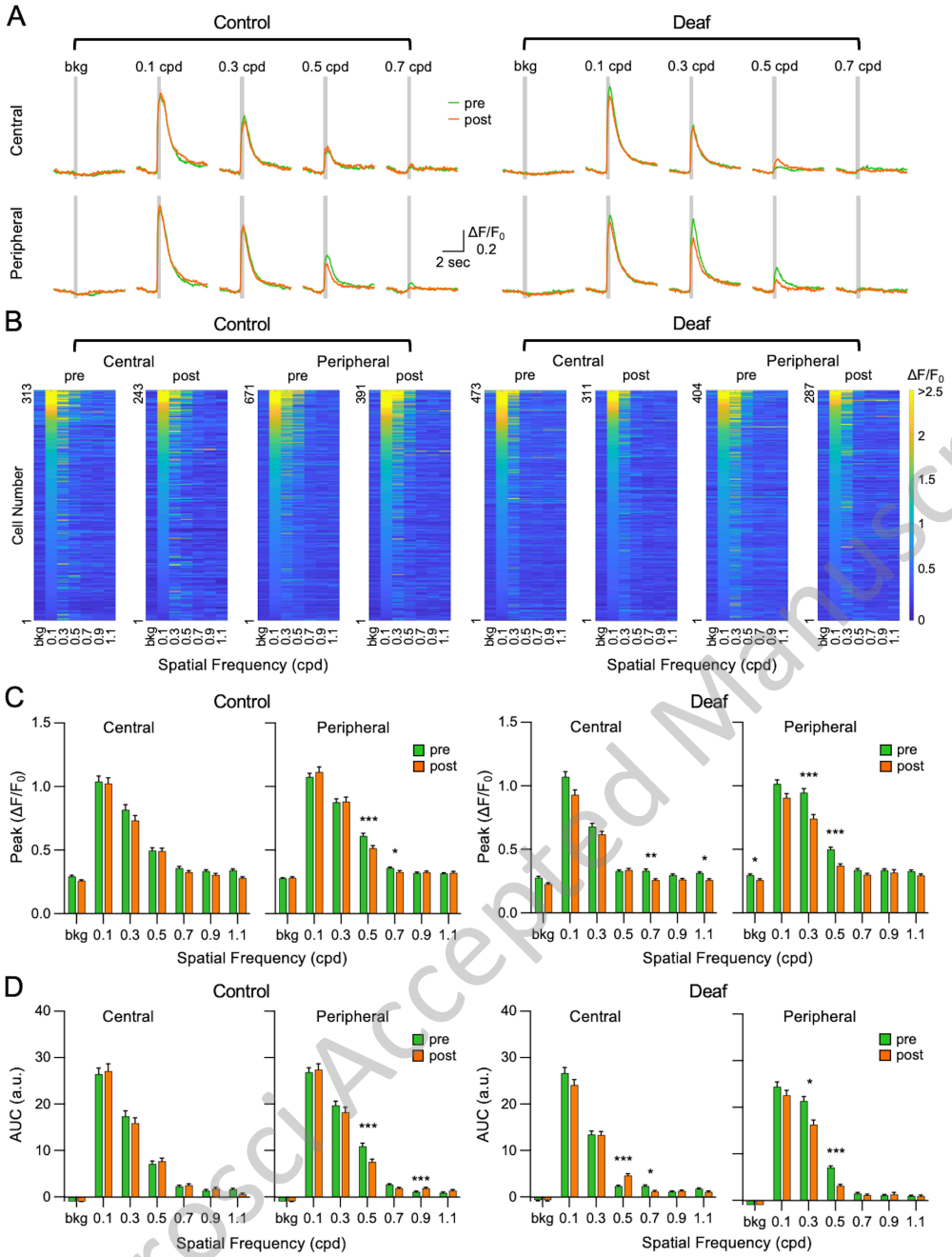
JNeurosci Accepted Manuscript



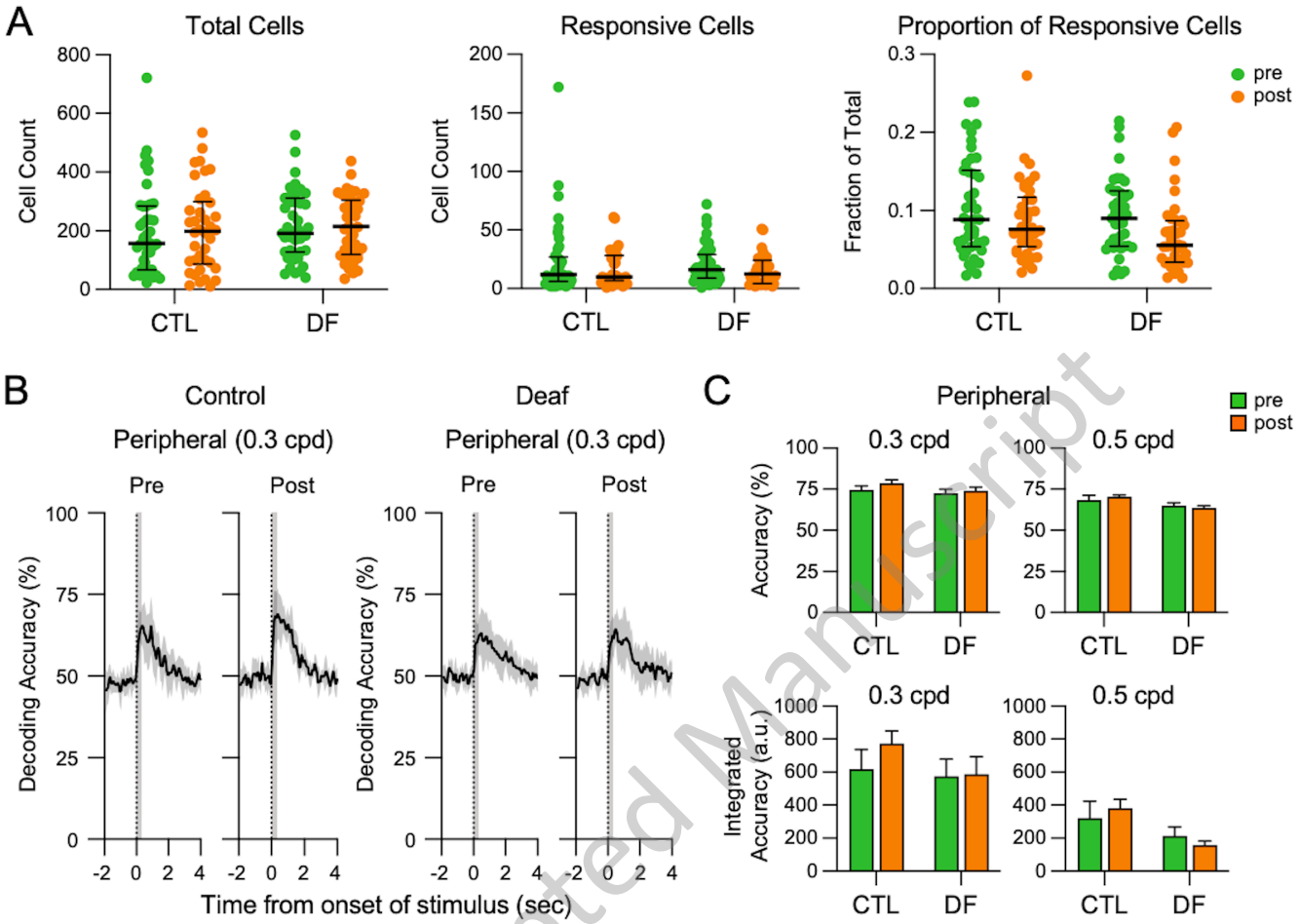




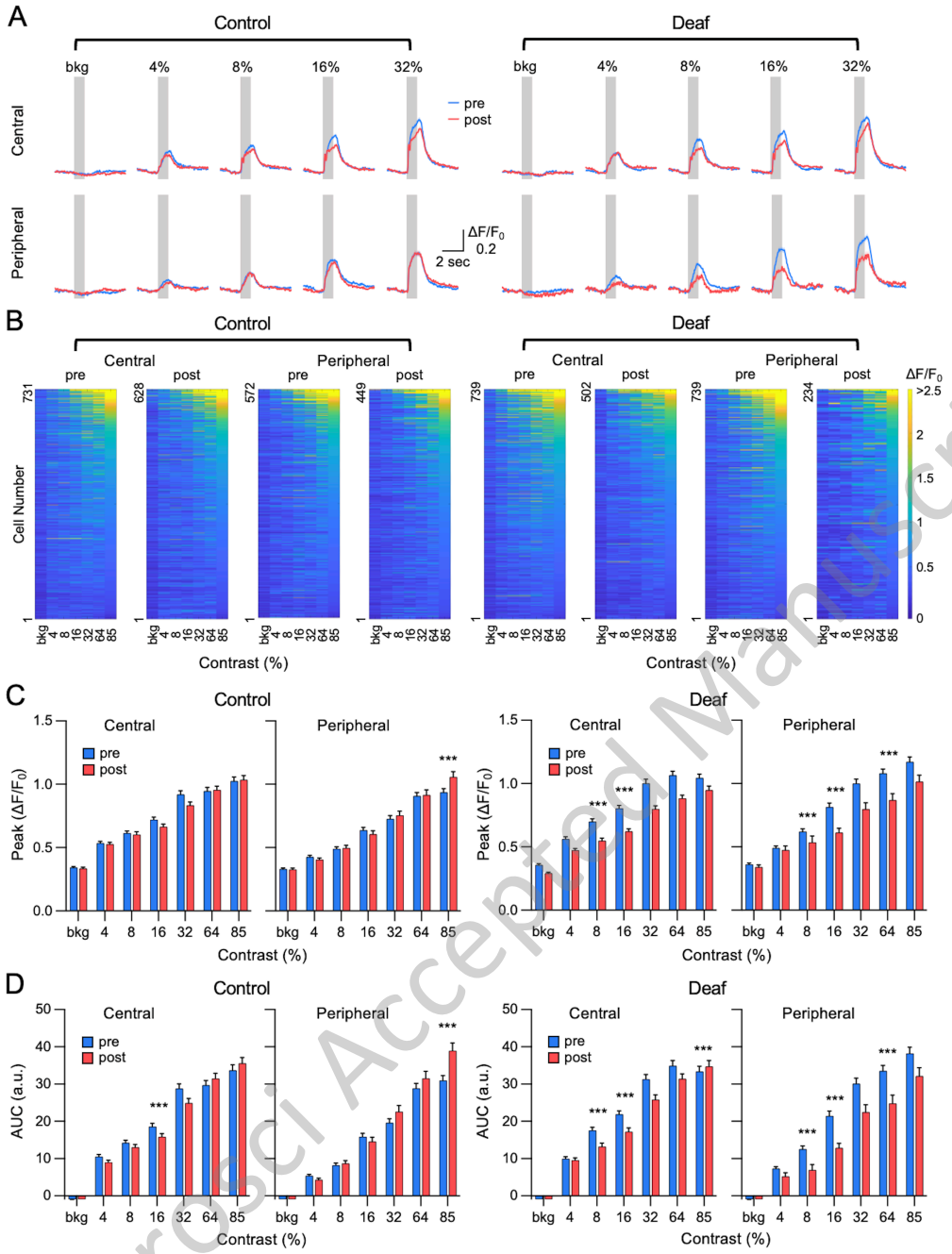
JNeurosci Accepted Manuscript



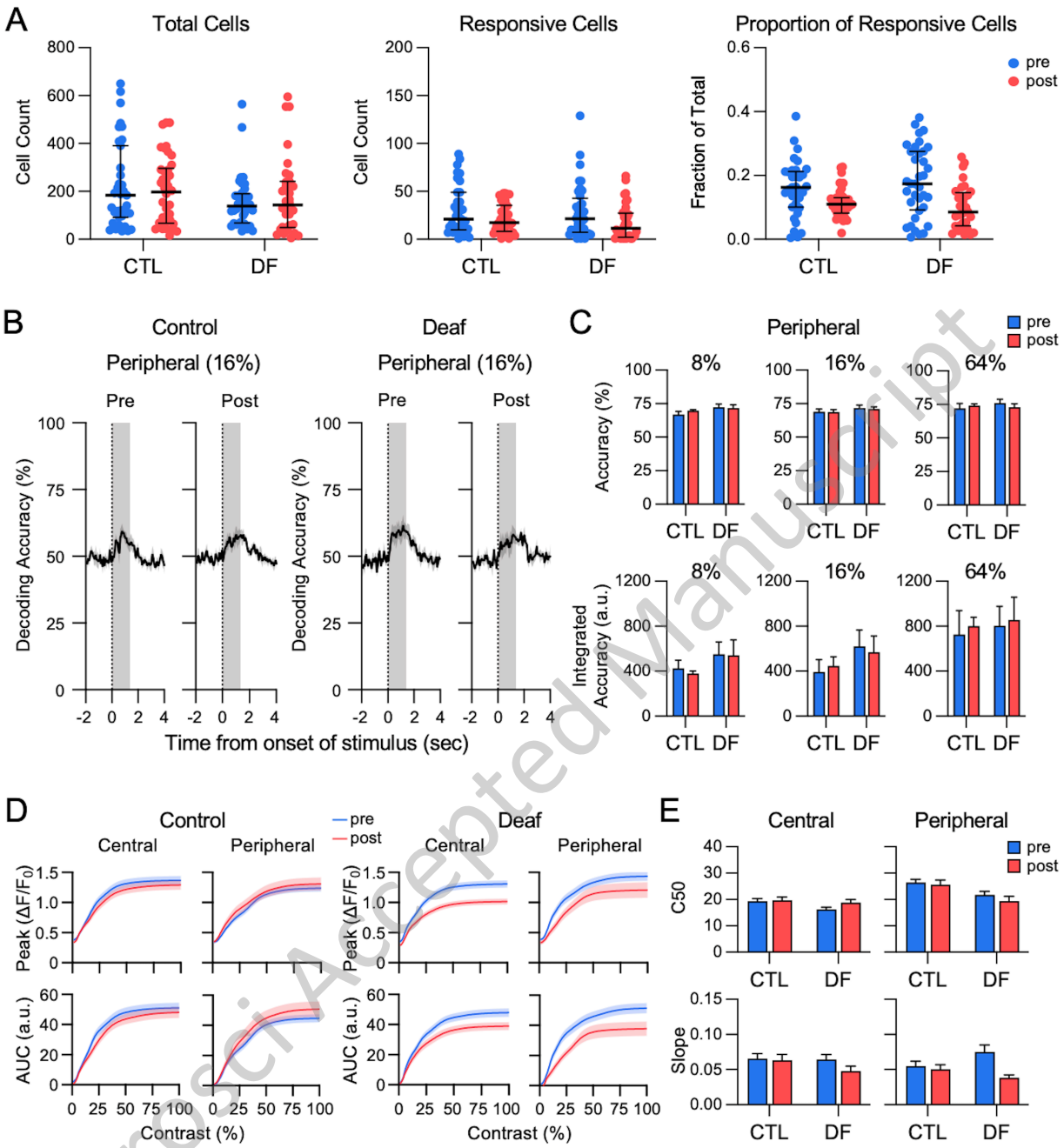
JNeurosci Accepted Manuscript



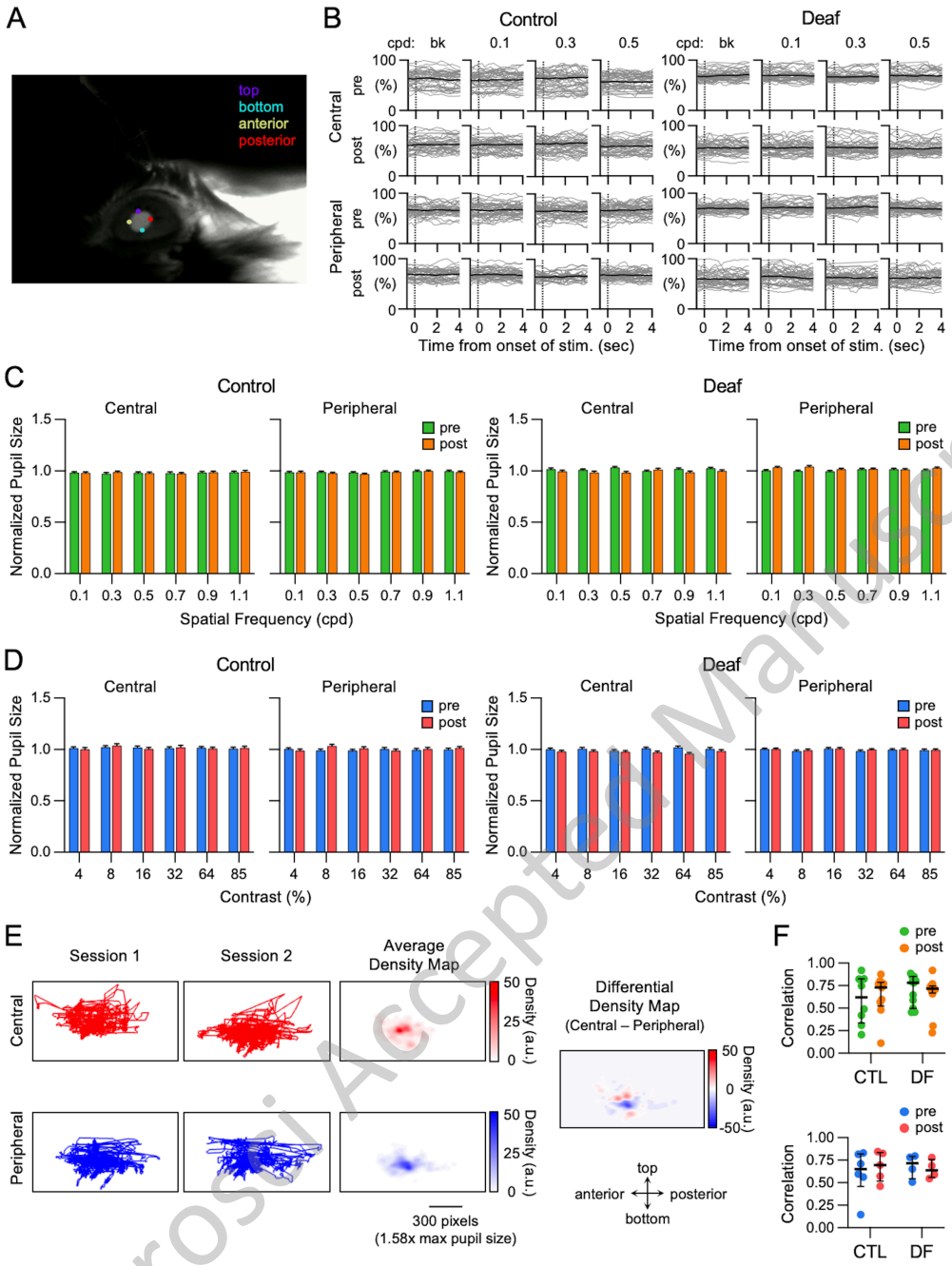
JNeurosci Accepted Manuscript



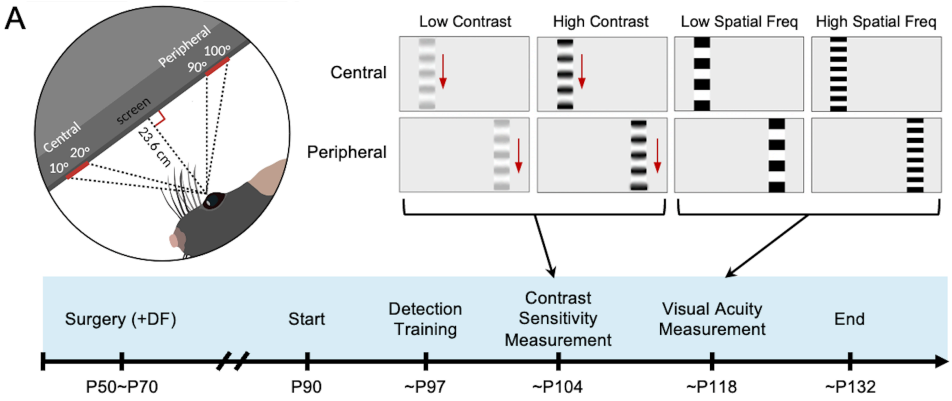
JNeurosci Accepted Manuscript

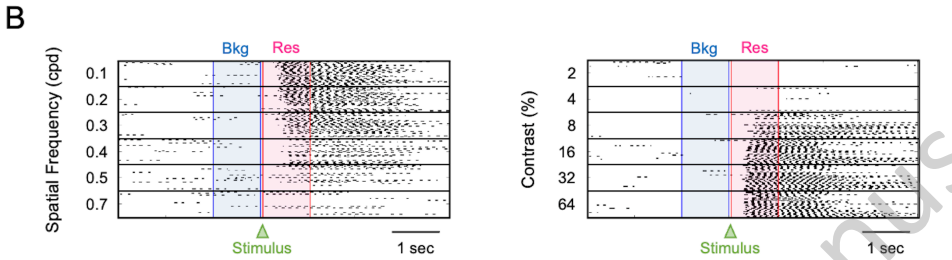


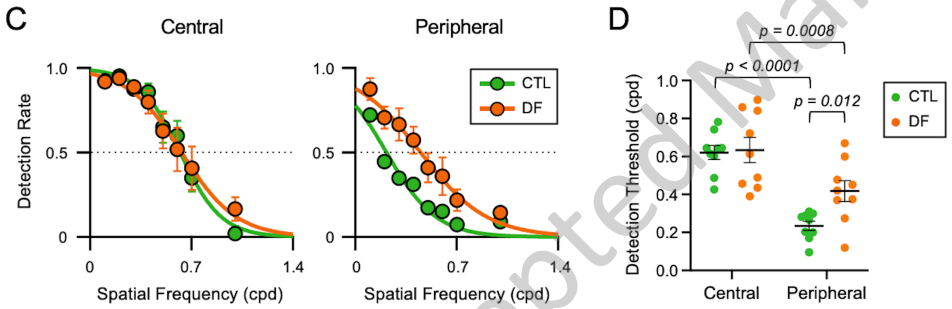
JNeurosci Accepted Manuscript

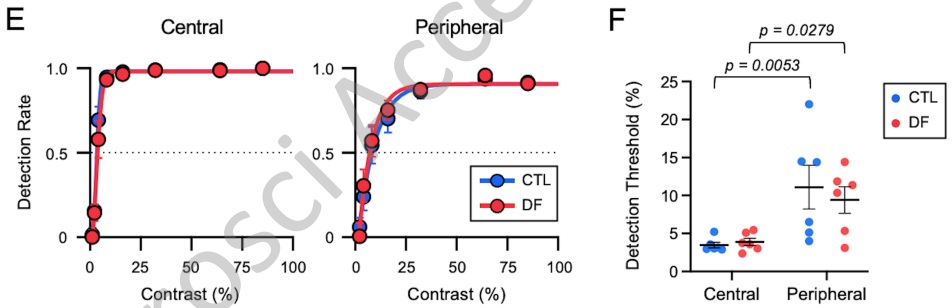


JNeurosci Accepted Manuscript









JNeurosci Accepted Manuscript